UC Berkeley
UC Berkeley Previously Published Works

Title
Optimized expansion microscopy reveals species-specific spindle microtubule organization in Xenopus egg extracts

Permalink
https://escholarship.org/uc/item/33v6254q

Journal
Molecular Biology of the Cell, 36(6)

ISSN
1059-1524

Authors
Guilloux, Gabriel
Kitaoka, Maiko
Mocaer, Karel
et al.

Publication Date
2025-06-01

DOI
10.1091/mbc.e24-09-0421

Copyright Information
This work is made available under the terms of a Creative Commons Attribution License, available at https://creativecommons.org/licenses/by/4.0/

Peer reviewed

eScholarship.org Powered by the California Digital Library
University of California

MBoC | ARTICLE

Optimized expansion microscopy reveals species-specific spindle microtubule organization in *Xenopus* egg extracts

Gabriel Guilloux[a], Maiko Kitaoka[b,†], Karel Mocaer[a,‡], Claire Heichette[a], Laurence Duchesne[a], Rebecca Heald[b], Thierry Pecot[c], and Romain Gibeaux[a,*]

[a]Univ Rennes, CNRS, IGDR (Institute of Genetics and Development of Rennes) – UMR 6290, Rennes F-35000, France; [b]Department of Molecular and Cell Biology, University of California, Berkeley, CA 94720; [c]Univ Rennes, SFR Biosit – UMS 3480 – US 018, Rennes F-35000, France

ABSTRACT **The spindle is key to cell division, ensuring accurate chromosome segregation. Although its assembly and function are well studied, the mechanisms regulating spindle architecture remain elusive. Here, we investigate spindle organization differences between *Xenopus laevis* and *tropicalis*, leveraging expansion microscopy (ExM) to overcome conventional imaging limitations. We optimized an ExM protocol tailored for *Xenopus* egg extract spindles, refining fixation, denaturation, and gelation to achieve higher resolution while preserving spindle integrity. Our protocol enables preexpansion immunofluorescence and is seamlessly compatible with both species. To quantitatively compare microtubule organization in expanded spindles between the two species, we developed an analysis pipeline that is able to characterize microtubule bundles throughout spindles. We show that *X. laevis* spindles exhibit overall a broader range of bundle sizes, while *X. tropicalis* spindles contain mostly smaller bundles. Although both species show larger bundles near the spindle center, *X. tropicalis* spindles otherwise consist of very small bundles, whereas *X. laevis* spindles contain more medium-sized bundles. Altogether, our work reveals species-specific spindle architectures and suggests their adaptation to the different spindle size and chromatin amount. By enhancing resolution and minimizing artifacts, our ExM approach provides new insights into spindle morphology and a robust tool for further studying these large cellular assemblies.**

SIGNIFICANCE STATEMENT

- Correct spindle morphology is key to its function; however, traditional microscopy methods limit our view of spindle architecture.
- This study addresses the gap in resolving detailed spindle microtubule organization by using expansion microscopy to reveal previously unobservable details of spindle morphology in egg extracts of two *Xenopus* species (*X. laevis* and *X. tropicalis*).
- This approach provides unprecedented clarity on microtubule arrangement and variations in spindle architecture.
- This work establishes a new protocol for high-resolution imaging of spindle structures, offering insights into how spindle architecture is adapted in differently sized spindles to ensure proper function.

Monitoring Editor
Matt Good
University of Pennsylvania

Received: Sep 25, 2024
Revised: Apr 7, 2025
Accepted: Apr 18, 2025

Challenge

Cross-Species

Instructional Resource

New Methods

INTRODUCTION

During cell division, the spindle plays a key role in ensuring the faithful segregation of the genetic material from the mother to daughter cells. This highly dynamic and self-organized structure is composed of thousands of microtubules and hundreds of other different proteins (Sauer *et al.*, 2005), which together form a bipolar assembly that provides the necessary forces to align chromosomes and pull them toward opposite spindle poles. Therefore, any defects in this process can lead to aneuploidy, which is associated with numerous pathologies in humans (Chunduri and Storchová, 2019). Consequently, the spindle has been extensively studied across various models, significantly advancing our understanding of spindle assembly (Helmke *et al.*, 2013; Guilloux and Gibeaux, 2020). Interestingly, although its components and function are well conserved across species, spindle size and morphology vary dramatically (Crowder *et al.*, 2015). The precise mechanisms by which the spindle regulates its architecture and morphometrics remain incompletely understood.

The *Xenopus* egg extract is a well-established model for studying spindle assembly. This cell-free system was initially developed to investigate nuclear envelope formation and the initiation of DNA synthesis (Lohka and Masui, 1983). However, since then, it has proven to be highly versatile, allowing the assembly of cytoskeletal structures (Geisterfer *et al.*, 2021). Although extracts were originally prepared from eggs of the African clawed frog, *Xenopus laevis*, the system has been adapted to various frog species, including *X. tropicalis*, *X. borealis,* and *Hymenochirus boettgeri* (Brown *et al.*, 2007; Kitaoka *et al.*, 2018; Miller *et al.*, 2019). Notably, compared with *X. laevis*, these species show different spindle sizes and architectures. In this study, we focus on the differences between the *X. laevis* and *X. tropicalis* spindles. Indeed, compared with *X. laevis, X. tropicalis* spindles are shorter (Brown *et al.*, 2007), display increased microtubule density at their poles (Helmke and Heald, 2014), and have more stable kinetochore fibers in the absence of the katanin enzyme (Loughlin *et al.*, 2011), making their comparison a powerful tool for elucidating the principles of spindle architecture regulation. Some species-specific differences, such as the severing activity of katanin (Loughlin *et al.*, 2011), dynamic properties of tubulins (Hirst *et al.*, 2020), and the TPX2/Eg5 interaction (Helmke and Heald, 2014), have been shown to contribute to global spindle size scaling between these two *Xenopus* species. However, a detailed comparison of spindle microtubule organization at much smaller scale has yet to be conducted.

Although individual microtubules have a diameter of about 25 nm and can reach several micrometers in length, the spindle they organize and densely occupy ranges from about 25 µm in length for *X. tropicalis* to about 40 µm for *X. laevis*. In this context, conventional light microscopy lacks the resolution to detail the organization of single microtubules within the spindle. Super-resolution techniques have continuously pushed the diffraction limit to significantly improve resolution (Sahl *et al.*, 2017), even reaching the nanometer scale (Balzarotti *et al.*, 2017). However, it requires specific equipment, fluorophores, and imaging conditions. On the other hand, electron microscopy can distinguish individual microtubules even when bundled at the ultrastructural scale, and has been used to image and reconstruct spindles from various species, including the yeasts *Schizosaccharomyces pombe*, *Saccharomyces cerevisiae,* and *Ashbya gossypii* (Höög *et al.*, 2007; Gibeaux *et al.*, 2012), the worm *Caenorhabditis elegans* (Redemann *et al.*, 2017), and human HeLa cells (Kiewisz *et al.*, 2022). Unfortunately, this technique is laborious and time-consuming, and sample size is greatly limiting, such that the largest reconstructed spindles mentioned above are not even half the length of the *X. laevis* spindle. Previous attempts to image the whole *X. laevis* spindle faced significant challenges, such as the segmentation and tracking of thousands of microtubules within the spindle across dozens of sections and the extremely large datasets generated (Heiligenstein, 2011). Even if electron microscopy could be used to image one *X. laevis* spindle, it would be a much greater challenge to image several across various perturbed conditions to allow comparison.

For these reasons, we turned toward expansion microscopy (ExM), which enhances spatial resolution by physically enlarging the sample, allowing it to be imaged using conventional microscopes. The original ExM protocol used a trifunctional label that included a methacryloyl group for free radical polymerization, a fluorophore for visualization, and an oligonucleotide that can hybridize to a complementary sequence attached to an affinity tag for recognizing biomolecules of interest. A swellable gel is then synthesized on the sample, incorporating the labels, followed by proteinase treatment to homogenize mechanical properties, and subsequent dialysis in water to expand the gel 4-fold (Chen *et al.*, 2015). Since its development, various alternative protocols have been proposed to adapt ExM depending on the sample characteristics, introducing new features that have been widely adopted in later studies. For example, proExM introduced succinimidyl ester of 6-((acryloyl) amino) hexanoic acid (AcX) to anchor biomolecules directly into the polymeric gel by specifically adding acrylamides on primary amines (Tillberg *et al.*, 2016). Due to significant protein loss caused by proteolytic digestion, the MAP protocol replaced it with thermal denaturation at 95°C in the presence of SDS (Ku *et al.*, 2016). Finally, another protocol, largely used nowadays, ultrastructure expansion microscopy (U-ExM), was developed to expand cellular ultrastructures using a mixture of formaldehyde and acrylamide to, like AcX, link acrylamides on primary amines to anchor biomolecules in the gel, an optimized acrylamide and sodium acrylate gel composition, and thermal denaturation (Gambarotto *et al.*, 2018).

Over the years, ExM has been adapted for imaging proteins, nucleic acids (Chen *et al.*, 2016), lipids (Wen *et al.*, 2020), and all biomolecules (Sun *et al.*, 2020). Moreover, ExM has also been successfully applied to various models and tissues, such as human kidney (Zhao *et al.*, 2017), *Drosophila melanogaster* (Jiang *et al.*,

This article was published online ahead of print in MBoC in Press (http://www.molbiolcell.org/cgi/doi/10.1091/mbc.E24-09-0421) on May 6, 2025.

Present addresses: †Whitehead Institute for Biomedical Research and Howard Hughes Medical Institute, Cambridge, MA; ‡Heidelberg University, Centre for Organismal Studies (COS), 69120 Heidelberg, Germany

Author contributions: G.G. performed all experiments and analyses presented in this article; M.K. and K.M. started the project and performed the qualitative initial optimization experiments; C.H. performed the early quantitative validations of optimizations and contributed to all subsequent experiments; R.G., R.H., and M.K. initially conceptualized the project; T.P. conceptualized, developed and optimized the expanded spindle analysis workflow; R.G. supervised the project with help and inputs from L.D; R.G. and G.G. wrote the initial article with help from L.D., M.K., and R.H. All authors read and improved the article.

Conflicts of interest: The authors declare no financial conflict of interest.

*Address correspondence to: Romain Gibeaux (romain.gibeaux@univ-rennes.fr).

Abbreviations used: AcX, succinimidyl ester of 6-((acryloyl) amino) hexanoic acid; ExM, expansion microscopy; PBSI, PBS supplemented with 0.1% (vol/vol) IGEPAL CA-630.; RMS, root-mean-square; ROI, region of interest; U-ExM, ultrastructure expansion microscopy.

© 2025 Guilloux *et al*. This article is distributed by The American Society for Cell Biology under license from the author(s). Twelve months after publication it is available to the public under an Attribution–Noncommercial–Share Alike 4.0 Unported Creative Commons License (http://creativecommons.org/licenses/by-nc-sa/4.0).

"ASCB®," "The American Society for Cell Biology®," and "Molecular Biology of the Cell®" are registered trademarks of The American Society for Cell Biology.

2018), *C. elegans* (Park *et al.*, 2019), *Arabidopsis thaliana* (Kao and Nodine, 2019), and fungi (Götz *et al.*, 2020). Nevertheless, ExM adaptations were often necessary to account for the mechanical properties of the sample and this complexity increases when mechanical characteristics vary within the sample itself. Indeed, different cellular organelles can exhibit varying expansion factors within the same cell (Büttner *et al.*, 2021). As the *Xenopus* egg extract spindles are a unique subcellular structure because of their large size and high density of cross-linked microtubules, we reevaluated ExM parameters, inspired by these different protocols.

Here, we successfully adapted ExM to faithfully maintain *Xenopus* egg extract structures, and ultimately analyzed the morphometric differences between *X. laevis* and *X. tropicalis* spindles with unprecedented detail. We showed that, overall, *X. laevis* spindles exhibit a broader range of microtubule bundle sizes, while *X. tropicalis* spindles are more limited to smaller bundles. We moreover revealed that, while both species favor similar larger bundle sizes near and at the spindle center, *X. tropicalis* spindles are typically built from very small bundles, and *X. laevis* spindles from medium-sized bundles in spindle regions between the poles and the midzone. Further analysis of the contribution of different spindle parameters also suggests that microtubule organization in *X. tropicalis* is modified upon an increase in size or DNA amount.

RESULTS

Validation of the ExM protocol on *Xenopus* egg extract spindles

We assembled spindles in *Xenopus* egg extracts supplemented with rhodamine-labeled tubulin (Figure 1A), fixed and spun them down onto coverslips (Figure 1B) as described previously (Hannak and Heald, 2006). To compare the same spindles before and after expansion and validate the tested conditions, we developed a homemade holed metal slide. This slide allowed us to image the coverslip and then recover it for ExM (Figure 1C). It was also essential to calculate the expansion factor for each spindle individually, the so-called local expansion factor, rather than assessing a global expansion factor by measuring the size of the gel before and after expansion, what was previously determined as the best practice (Truckenbrodt *et al.*, 2019). Importantly, we optimized our protocol to preserve the rhodamine signal of tubulins to directly and faithfully image microtubules without the need for immunofluorescence. In addition, we aimed to retain the postcentrifugation fixation that enables pregelation immunofluorescence of other proteins and thus increases the options for the immunodetection of proteins of interest. To incorporate biomolecules of interest into the gel, AcX was chosen for its specificity, efficiency, and simplicity as well as to limit the use of aldehydes and prevent potential unwanted side reactions. We then began our optimization by comparing the gelation solutions from the original ExM protocol and the one from the U-ExM that uses the same components but in different proportions (Figure 1C). After polymerization, two homogenization methods were also tested: proteinase K digestion as in the ExM protocol or 95°C denaturation in the presence of SDS as in the MAP (Ku *et al.*, 2016) and U-ExM protocols (Figure 1C).

To assess the above-mentioned variations, we quantitatively compared four conditions: ExM gel with proteinase K digestion (Figure 2A), U-ExM gel with thermal denaturation (Figure 2B), ExM gel with thermal denaturation (Figure 2C), and U-ExM gel with proteinase K digestion (Figure 2D). Expansion factors were measured and their variability assessed by aligning the same spindles before and after expansion. It was first observed that proteolytic digestion (Figure 2, A and D) induces slightly greater expansion but more variability compared with denaturation (Figure 2, B and C). Additionally, for the same disruption procedure, U-ExM gels displayed slightly higher expansion factors compared with ExM gels.

Next, the preservation of rhodamine-labeled tubulin fluorescence distribution was analyzed by measuring tubulin intensity along the axis of the spindle from pole-to-pole in both pre- and postexpansion spindles (top images for each condition in Figure 2). It appeared evident that proteolytic digestion resulted in decreased intensity in the center of the expanded spindle (blue and red curves in Figure 2, A and D), and to a lesser extent, in the ExM gel with thermal denaturation condition (blue and red curves in Figure 2C). In contrast, the U-ExM gel with thermal denaturation condition (blue and red curves in Figure 2B) showed a similar distribution of tubulin across both unexpanded and expanded spindles.

Finally, to assess possible distortions due to expansion, we calculated the root-mean-square (RMS) error as described in the original ExM protocol (Chen *et al.*, 2015). The unexpanded spindle images were magnified 4-fold and rigidly aligned by rotating and resizing them to match the expanded spindle images using the Elastix software. Nonrigid alignment with allowed local deformations was then performed to perfectly fit the two images. For each alignment, the applied transformations were registered and applied to expanded spindles to generate two new images, one having undergone rigid transformations, and the other having undergone rigid and nonrigid transformations. These two images were aligned in Mathematica (bottom left images for each condition in Figure 2) and the differences between the two images (representing the deformations due to expansion) were calculated in a vector field (bottom right images for each condition in Figure 2) and given as RMS error length measurement (orange curves in Figure 2). Doing so, we observed that proteolytic digestion resulted in higher RMS errors compared with thermal denaturation, indicating more distortions.

Based on these observations, we decided to proceed with the U-ExM gel and thermal denaturation (Figure 2B) as it provided significant expansion with minimal variations, preservation of the rhodamine-labeled tubulin signal across the spindle, and acceptable distortions, with a 1 µm measurement error on 40-µm length, representing a 2.5% distortion error, which is within most published protocols' range of 1 to 5% (Chen *et al.*, 2015; Ku *et al.*, 2016; Tillberg *et al.*, 2016; Gambarotto *et al.*, 2018).

Expansion successfully increases resolution

To assess the increased resolution, the same spindles were imaged before and after expansion with confocal microscopy equipped with a gain of resolution technology. These spindles were first observed in three dimensions using Napari software to visualize the overall gain of resolution. Individual microtubule bundles, corresponding to few parallel microtubules associated together by cross-linkers or motors, could easily be distinguished within spindles and the DNA was correctly expanded (Figure 3A). To demonstrate this increased resolution, we focused on spindle pole regions where thin lines of fluorescence, corresponding to individual microtubules or bundles, were clearly distinguishable, and plotted the fluorescence distribution across microtubule bundles and observed that microtubules were more clearly resolved after expansion (Figure 3B). Furthermore, to analyze microtubule bundle organization within the spindle at this increased resolution, we developed an analysis workflow enabling us to reconstruct the spindle in three dimensions and spatially rotate it, using selected pole coordinates, to align the pole-to-pole axis with the *z*-axis (Supplemental

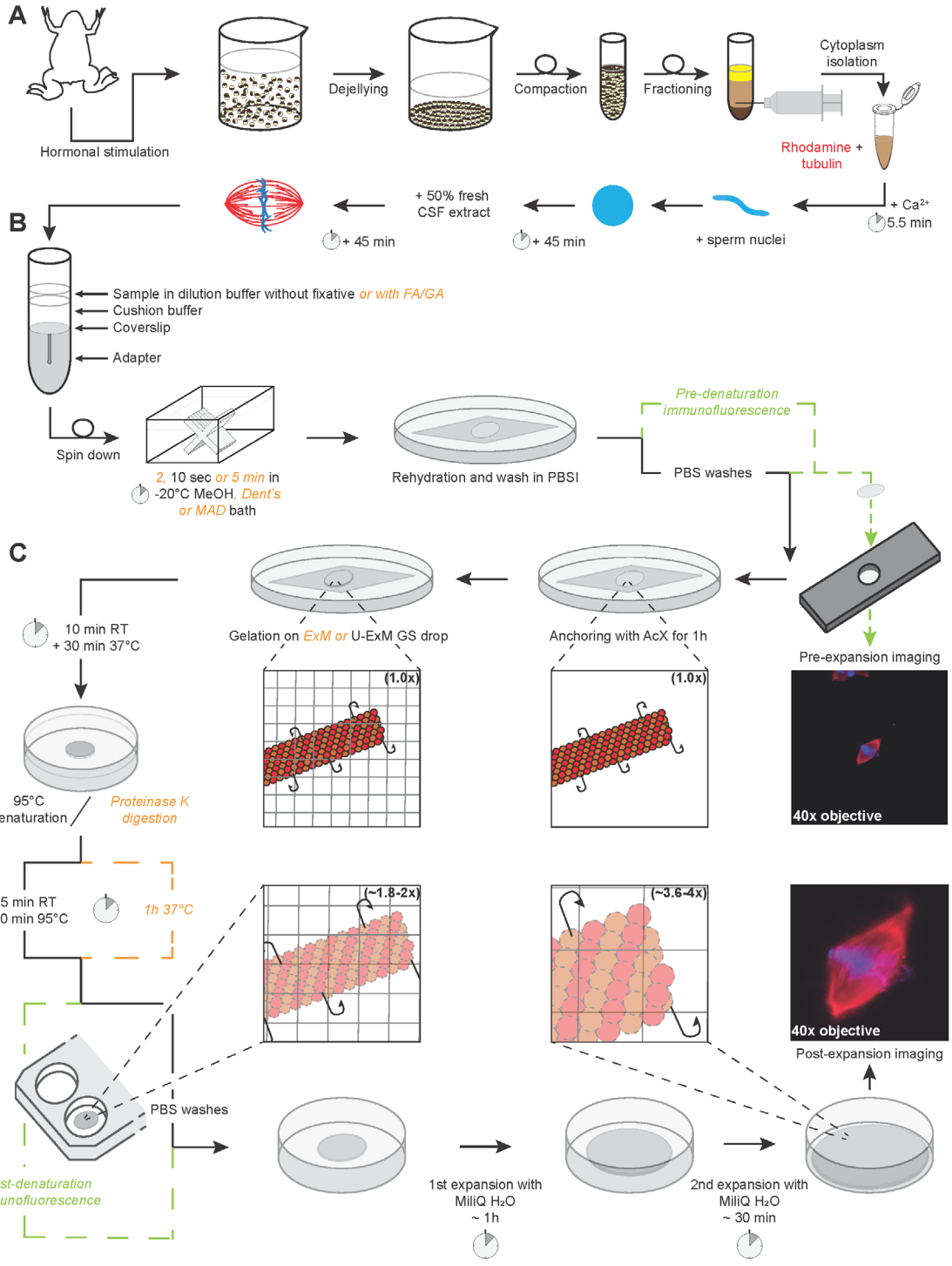


FIGURE 1: Sample processing workflow for ExM of *Xenopus* egg extract spindles. (A) Preparation of egg extract spindles for ExM, including major steps of egg extract preparation and spindle assembly. (B) Sample in dilution buffer, with or without fixatives, is deposited on cushion buffer to spin-down spindles onto a coverslip placed at the top of the adapter. Following the centrifugation, the coverslip is immersed inside a bath of methanol or other fixative mixtures from 2 s to 5 min, and finally rehydrated in PBSI. (C) ExM-specific steps from anchoring and gelation to disruption and expansion. Right images show the same spindle before (top) and after (bottom) expansion with rhodamine-labeled tubulin in red and DNA in blue. Note that immunofluorescence for preexpansion imaging is performed after sample fixation and before anchoring and that immunofluorescence for postexpansion imaging is done after disruption and before expansion for imaging. If these steps are not performed, they are replaced by PBS washes. (CSF, cytostatic factor-arrested; FA, formaldehyde; MeOH, methanol; Dent's, mix of methanol and DMSO; MAD, mix of methanol, acetone, and DMSO; PBSI, PBS 0.1% IGEPAL CA-630; AcX, 6-((acryloyl) amino) hexanoic acid, succinimidyl ester; ExM, expansion microscopy; U-ExM, ultrastructure ExM; RT, room temperature).

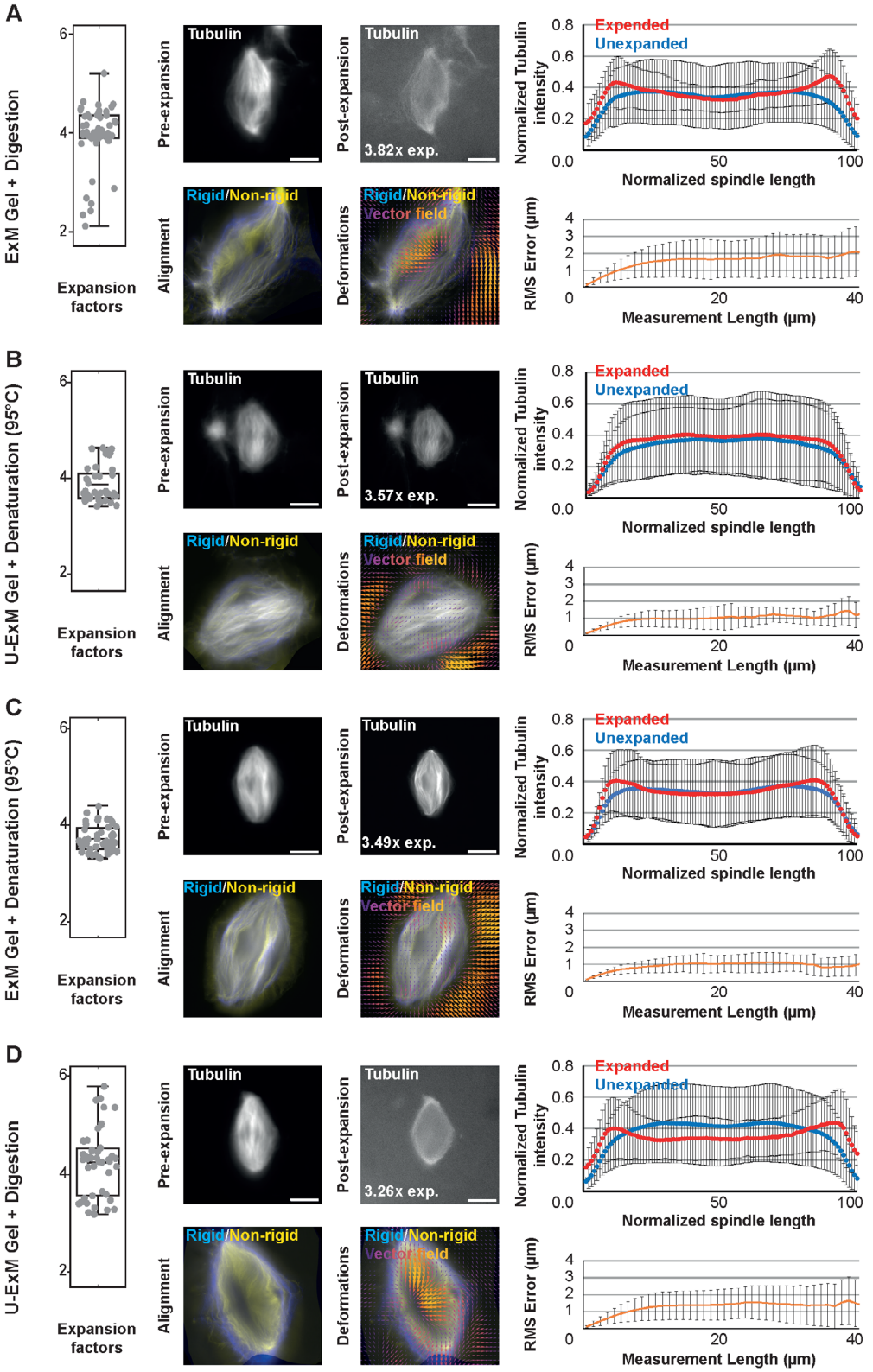


FIGURE 2: Comparison of expansion factors, rhodamine-labeled tubulin intensity distribution, and RMS error between the different expansion protocols. The four conditions tested on *X. laevis* spindles differing in the acrylamide composition of the gels and the nature of the disruption method are shown: (A) ExM gel + proteinase K digestion, (B) U-ExM gel + thermal denaturation, (C) ExM gel + thermal denaturation, and (D) U-ExM gel + proteinase K digestion. Left panels are boxplots showing individual spindle expansion factors ($n = 51$, $n = 41$, $n = 47$, and $n = 47$ spindles from four egg extracts, respectively, for A–D), the center line is the mean, the box indicates the 25 to 75% quantiles and the error bars the minimum and maximum values. Average expansion factors were (A) 3.94 ± 0.63, (B) 3.86 ± 0.37,

Figure S1). As a result, we are able to cross-section the spindle at various chosen positions and apply a specifically trained Stardist model to segment microtubule bundles, and determine their individual area and fluorescence intensity. Applying this analysis on the same spindles imaged before and after expansion, we found that bundles were more individualized and more of them could thus be detected after expansion, confirming the increased resolution (Figure 3C). Moreover, as a control to confirm that microtubule bundling was not due to spindle fixation, we imaged unfixed spindles, either live (Supplemental Figure S2A) or right after centrifugation in glycerol-containing mounting medium (Supplemental Figure S2B), and observed the presence of bundles in both conditions. However, microtubules appeared buckled within the spindles. To confirm that this was not due to our expansion protocol, we compared the undulations in unexpanded and expanded spindles (Figure 3D). As microtubules were already buckled before expansion, we concluded that this was likely due to the fixation protocol. Indeed, aldehydes present in our dilution buffer are known to induce wavy microtubules (Cross and Williams Jr., 1991), and methanol baths used can cause cell shrinkage (Melan, 1999), potentially similarly shrinking spindles and thus causing microtubule buckling.

Therefore, we attempted to improve the classical spin-down protocol by modifying various parameters. To keep postcentrifugation fixation to enable preexpansion immunofluorescence, we began by changing the formaldehyde incubation duration, using dilution buffer with or without detergent, changing the postmethanol rehydration agent, and reducing the centrifugation speed (Supplemental Figure S3). We also varied the formaldehyde concentration, removing or replacing it with glutaraldehyde at different concentrations (Supplemental Figure S4, A and B). Although fixing spindles with glutaraldehyde seemed promising before expansion, with straighter microtubules, these were deformed and appeared crushed after expansion (Supplemental Figure S4C), displaying increased distortions with more than 10% error (Supplemental Figure S4D). Moreover, stronger fixation resulted in less successful incorporation within the gel. Altogether, these attempts led us to decide to remove any fixative from the dilution buffer in our final conditions and supported our choice of AcX for anchoring egg extract spindles.

Minimal postcentrifugation fixation better preserves spindle integrity

In parallel to precentrifugation fixation optimization tests, we optimized the postcentrifugation methanol fixation. We tested alternatives, including Dent's fixative (80% methanol, 20% DMSO; Dent *et al.*, 1989), MAD (40% methanol, 40% acetone, 20% DMSO; Gibeaux *et al.*, 2018), and a variant of the latter, MAD2 (60% methanol, 20% acetone, and 20% DMSO), with the objective of tempering the methanol dehydration (Figure 4). Visually, the MAD and Dent's alternatives appeared superior in terms of microtubule preservation, with more individualized bundles. Importantly, both the tubulin distribution intensity along spindles and RMS errors were similar across all conditions (Figure 4A), suggesting that the expansion was not affected by these modifications. Only the expansion factors of samples fixed with alternative baths were significantly higher compared with the control (Figure 4B).

Because microtubule buckling was the most evident indicator of protocol issues, microtubule average curvature was measured using the Fiji plugin Kappa. Although microtubules seemed less curved with less variability for MAD bath (0.23 $\mu m^{-1} \pm 0.11$ vs. 0.25 $\mu m^{-1} \pm 0.14$; average $\pm$ SD), consistent with more individualized bundles, no improvement was statistically significant at this level (Figure 4C). The other parameter influenced by chemical fixation is shrinkage of the fixed structures. We therefore measured unexpanded spindle lengths in each condition but did not see any significant differences, except from an even greater reduction in size from Dent's fixative condition (Figure 4D). Together, although the MAD fixation seemed to maintain better individualized microtubule bundles, these results do not indicate a clear improvement of the fixation protocol. However, as the MAD mix aimed to temper the strong dehydration and extraction effect of methanol, we wondered whether we could get significantly better results by reducing the methanol fixation duration.

To test this idea, we reduced the duration of both control and MAD fixation from 5 min to 2 s. Additionally, from these new conditions on, based on our previous results (Supplemental Figures S3 and S4), we removed the fixative from the dilution buffer and directly assessed the influence of postcentrifugation baths. Visually, microtubules appeared straighter and more individualized with reduced fixation durations. Of note, reduced durations also led to the disappearance of spindles between preexpansion to postexpansion imaging, likely due to them washing off the coverslip during washes, which was most striking in the 2 s condition.

We measured the distribution of rhodamine-labeled tubulin intensity along the spindles. For both methanol 10 s and MAD 10 s conditions (Figure 5A), the overlap was nearly perfect. Yet, we observed an increase in distortions as fixation duration decreased, with the RMS error approaching 2 μm in the methanol 10 s condition and almost 3 μm in the MAD 10 s condition (Figure 5A), and more than 3 μm in the 2 s conditions (Figure 5A). Interestingly, the methanol 10 s condition showed an increased expansion factor while it decreased in its MAD counterpart (Figure 5B).

Importantly, the shorter duration conditions resulted in less curved microtubules (Figure 5C), and longer spindle lengths (Figure 5D). We found a positive correlation between average spindle microtubule curvature and average spindle shrinkage (Figure 5E; $R^2 = 0.74$), suggesting that spindle shrinking resulting from chemical fixations led to microtubule buckling.

Taken together, postcentrifugation fixation with methanol for 10 s gave the best compromise, (1) sufficiently fixing the spindles onto the coverslip with (2) moderate spindle shrinkage, (3) reasonable distortion error below 5%, which remains within the range of published protocols, (4) the straightest microtubules of all conditions,

(C) 3.71 $\pm$ 0.27, and (D) 4.22 $\pm$ 0.67 (average value $\pm$ SD). For each, top images are representative images of unexpanded (left) and expanded (right) spindles, with rhodamine-labeled tubulin shown in gray. The expansion factor of the shown spindle is indicated. On the right of the top images are the average normalized fluorescence intensity distributions $\pm$ SD for unexpanded (blue) and expanded (red) spindles. Bottom images show the alignment (left) made between rigid registration and nonrigid registration, and (right) the vector field of deformations calculated from the registrations. On the right of the bottom images, panels represent the RMS length measurement error as a function of measurement length for pre- versus postexpansion images. The orange line shows the average and the error bars, the SD ($n = 51$, $n = 41$, $n = 47$, and $n = 47$ spindles from four egg extracts, respectively, for A–D). Scale bars, 10 μm for unexpanded spindles and 40 μm for expanded spindles.

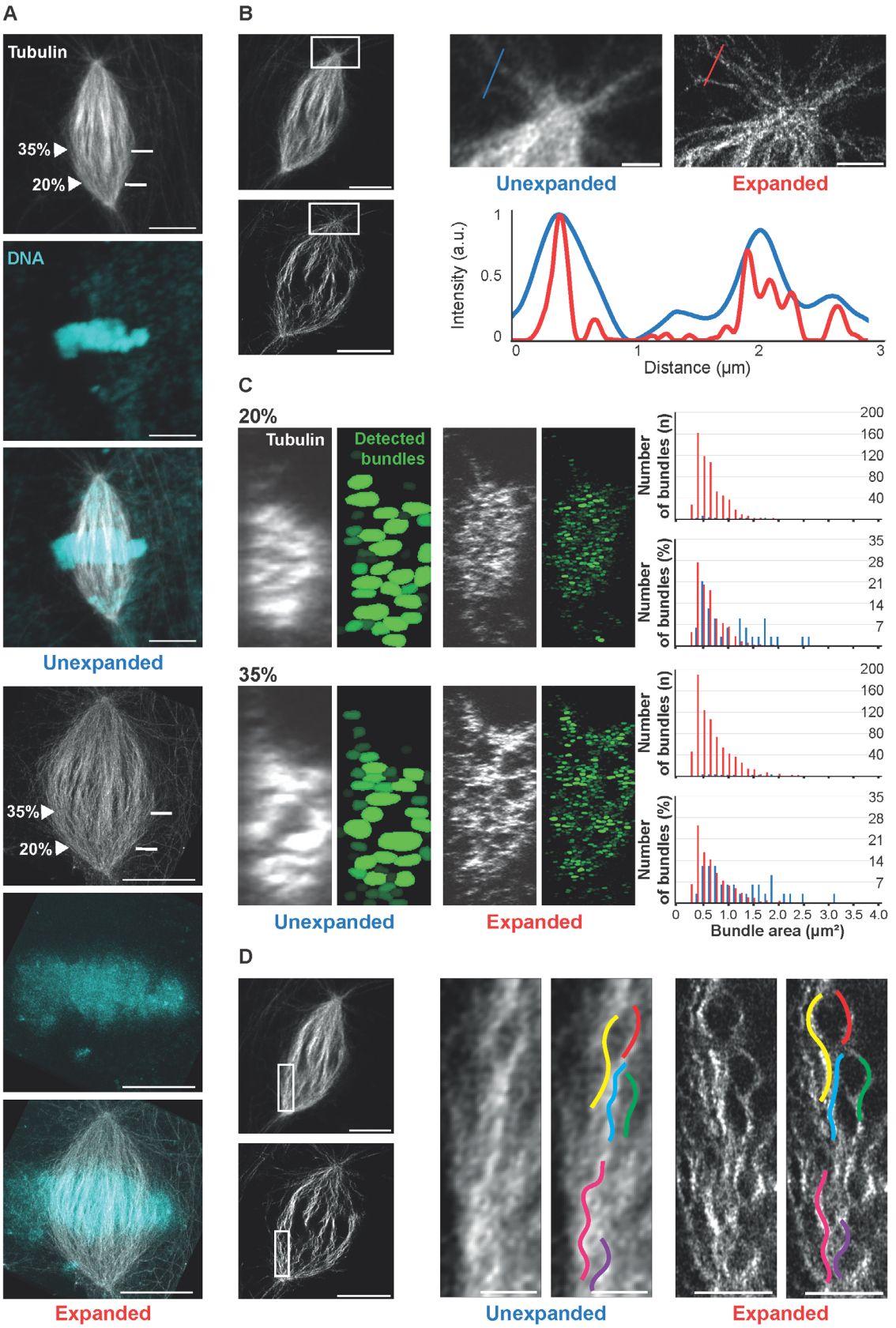


FIGURE 3: Analysis of resolution improvement and fixation artifacts. (A) Images from a 3D rendering in Napari showing an unexpanded (three top images) and expanded (three bottom images) *X. laevis* spindle with rhodamine-labeled tubulin signal (top), DNA signal (middle), and merged signals (bottom). Arrows and corresponding lines indicate the location of the spindle cross-sections shown in C. (B) Single *z* plane of the spindle shown in A, unexpanded (top) and

and (5) a perfect maintenance of the rhodamine-labeled tubulin fluorescence distribution. We therefore selected this fixation condition as our final fixation protocol, in which chemical fixation (no aldehydes and a short dehydration step) was effective and minimally deleterious.

One goal of our optimization was to enable preexpansion immunofluorescence. Indeed, although postexpansion immunofluorescence can be performed with our protocol as with any other ExM protocol, some antibodies are not functional after expansion, likely as a result of the denaturation step. This was the case for most antibodies routinely used in the laboratory for classical immunofluorescence analysis in *Xenopus* egg extract. To confirm that preexpansion immunofluorescence was still possible after 10 s of methanol fixation, we performed immunofluorescence using an antidynein antibody that displays a faint signal in classical immunofluorescence analysis and does not work for postexpansion immunofluorescence. (Supplemental Figure S5A). As expected with this antibody, a faint signal on the spindle with increased signal at the spindle poles was observed. After retrieving the coverslip, we applied our expansion protocol and imaged the gel using an epifluorescence microscope (Supplemental Figure S5B). The labeling was properly preserved after expansion, together with well-separated microtubule bundles. Moreover, the increased signal at the poles observed preexpansion appeared as separated puncta and few separated dots become visible within the spindle after expansion. These findings confirm that our protocol allows preexpansion immunofluorescence and suitable for antibodies that cannot be used for postexpansion immunofluorescence.

Individual microtubule bundles can be segmented from expanded spindles

With our final protocol in hand, we returned to high-resolution imaging and observed that, compared with spindles in Figure 3A, the spindle volume was better preserved and the microtubules were incomparably straighter and individualized (Figure 6A; Supplemental Movie S1). To measure the effective resolution under this condition, we analyzed microtubules, outside the spindles. Some of them appeared as dotted lines suggesting the separation of individual labeled-tubulin molecules on a single microtubule (rhodamine-labeled tubulin was added to the extract at 1:50 ratio). We measured the full-width at half-maximum of these isolated dots and obtained a value of 299.65 nm $\pm$ 3.88 ($n = 27$), corresponding to the *xy* resolution in our imaging conditions. Dividing this value by our expansion factor, we obtain an effective ExM *xy* resolution of 77.23 nm. It has to be clarified that as a confocal-based technology, the Airyscan resolution is not isotropic and ~3X lower in z (Wu and Hammer, 2021). Considering the expansion to be isometric, we can thus assume our spindle volumes to be of an ~230 nm effective ExM resolution in z.

Interestingly, we found that this protocol also perfectly preserved spindles assembled in *X. tropicalis* egg extracts (Figure 6B; Supplemental Movie S2). Yet, although the gain in resolution is clear, the difficulty of following individual bundles within the spindle volumes also becomes evident (Supplemental Movies S1 and S2). Hence, to decipher the architectural differences between the spindles of these two species at an unprecedented resolution, we used our analysis pipeline (Supplemental Figure S1) and segmented bundles to measure their area and fluorescence intensity, at different sections: the poles (5 and 95% sections), at the spindle center (50% section), and between these locations (at 20, 35, 65, and 80% sections). Since microtubules were labeled with rhodamine-labeled tubulin, it was expected that increased microtubule number in a bundle would increase bundle size and measured fluorescence intensity. Therefore, to assess the accuracy of our bundle detection, in addition to visual inspection, we plotted the cross-section area against the intensity for each detected bundles for *X. laevis* (Supplemental Figure S6A) and *X. tropicalis* (Supplemental Figure S6B). We observed a satisfactory linear relationship between these two parameters, with a dispersion likely resulting from various possible lengths of bundlers but not excluding the possibility of including individual microtubules close enough to be indistinguishable from each other at our resolution.

We analyzed the number of microtubule bundles in each section according to their area, from spindles of *X. laevis* (Figure 6C) and X. *tropicalis* (Figure 6D). A similar distribution between the two species was observed, with a majority of bundles being 0.5 to 1.0 μm^2, and a higher count for *X. laevis* as expected due to their respective spindle size. However, before further analyzing these data, we performed additional validations.

Although we could identify individual microtubules outside the spindle (Supplemental Figure S6C) to measure the spatial resolution achievable with our method, these were difficult to detect within the spindle due to the high density in microtubules (Supplemental Figure S6D). We thus wondered whether they were identified with our analysis pipeline as part of the detected bundles in xz. With our resolution, an isolated dot of rhodamine tubulin would have in xz an area of 0.212 μm^2 and an isolated expanded microtubule with all or most tubulin labeled would have in xz an area of about 0.314 μm^2. In this way, our algorithm was able to detect areas that are clearly individual microtubules (Table 1), suggesting that not all microtubules are part of bundles.

expanded (bottom). Magnified views of boxed regions in unexpanded and expanded spindles (top right). Profiles of tubulin intensity along the blue (unexpanded) and red (expanded) lines (bottom right). (C) For the top and bottom left panels with spindle sections indicated in top left corners as in A, the first image (from left to right) shows the tubulin fluorescent signal of cross-sectioned microtubule bundles within the unexpanded spindle cross-section. The second image shows only the bundles detected in the previous image by the ImageJ macro and color-coded according to their size using Qupath, smaller being darker and larger being brighter. The third image shows the tubulin fluorescent signal of cross-sectioned microtubule bundles at the same location in the same spindle after expansion. The fourth image shows only the bundles detected in the previous image by the ImageJ macro and color-coded according to their size using Qupath, smaller being darker and larger being brighter. Bar plots on the right show, for each indicated spindle section, the distribution of these detected bundles, according to their area, as number of bundles (op) and their relative abundance in percentage (bottom). Bundle areas are binned into classes of 0.125 μm^2. Each bin is named according to its upper range value. Sections at 20 and 35% were chosen because of high bundle densities able to reveal gain in resolution. (D) Single *z* plane of the spindle shown in A, unexpanded (top) and expanded (bottom). Magnified views of boxed regions in unexpanded and expanded spindles with colored curves traced on unexpanded (left) and expanded (right) microtubule bundles. Scale bars, 10 µm for unexpanded spindles and 40 µm for expanded spindles in A to C, 2 µm for magnified views of boxed regions showing unexpanded microtubules and 8 µm for expanded microtubules in B and C.

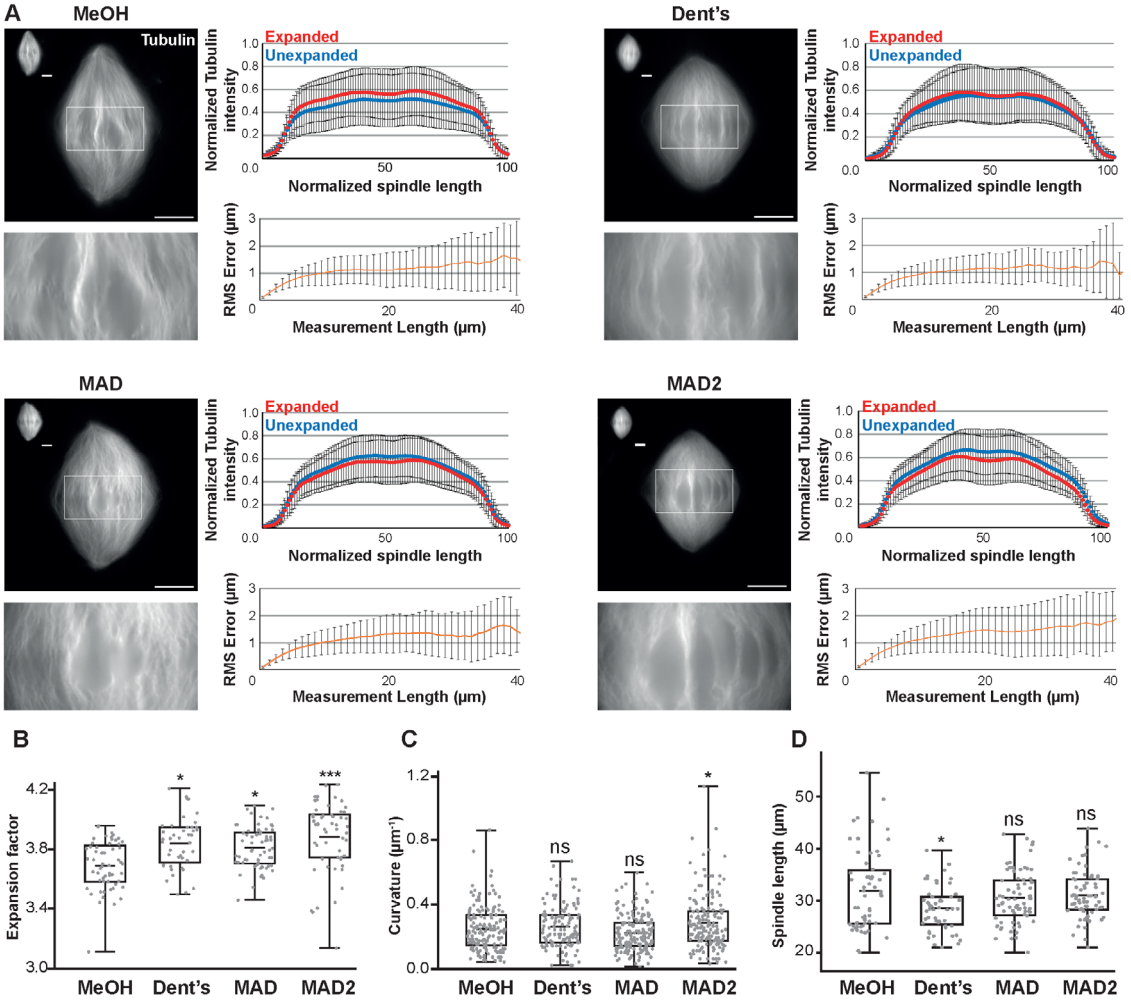


FIGURE 4: Evaluating the effects of changing the nature of the postcentrifugation fixation. (A) The four conditions tested on *X. laevis* spindles differing by the composition of the postcentrifugation fixation: MeOH (100% methanol), Dent's (80% methanol and 20% DMSO), MAD (40% methanol, 40% acetone, and 20% DMSO), and MAD2 (60% methanol, 20% acetone, and 20% DMSO). For each top left images show expanded spindles (rhodamine-labeled tubulin signal) and their corresponding unexpanded spindles in the top left corner of the image. Bottom left images are magnified views of boxed regions in top images. Top right panels are the average normalized fluorescence intensity distributions ± SD for unexpanded (blue) and expanded (red) ($n = 57$ spindles from six egg extracts, $n = 47$ spindles from five egg extracts, $n = 64$ from five egg extracts, and $n = 60$ spindles from six egg extracts, respectively, for MeOH, Dent's, MAD, and MAD2). Bottom right panels represent the RMS length measurement error as a function of measurement length for pre- versus postexpansion images. The orange line shows the average and the error bars, the SD ($n = 56$ spindles from six egg extracts, $n = 44$ spindles from five egg extracts, $n = 64$ spindles from five egg extracts, and $n = 54$ spindles from six egg extracts, respectively, for MeOH, Dent's, MAD, and MAD2). (B) Boxplots showing individual spindle expansion factors (same statistics as for RMS error study), the center line is the mean, the box indicates the 25 to 75% quantiles and the error bars the minimum and maximum values. Average expansion factors were MeOH: 3.68 ± 0.16, Dent's: 3.83 ± 0.17, MAD: 3.80 ± 0.14, MAD2: 3.88 ± 0.23 (average value ± SD). (C) Boxplots showing average curvature of microtubules measured by tracking individual microtubule bundles on expanded spindles ($n = 159$ microtubules, $n = 122$ microtubules, $n = 173$ microtubules, and $n = 168$ microtubules, respectively, for MeOH, Dent's, MAD, and MAD2), the center line is the mean, the box indicates the 25 to 75% quantiles and the error bars the minimum and maximum values. Average curvature were MeOH: 0.25 μm^{-1} ± 0.14, Dent's: 0.27 μm^{-1} ± 0.13, MAD: 0.23 μm^{-1} ± 0.11, MAD: 0.29 μm^{-1} ± 0.17 (average value ± SD). (D) Boxplots showing individual spindle length measured on unexpanded spindles ($n = 59$ spindles from six egg extracts, $n = 52$ spindles from five egg extracts, $n = 61$ spindles from five egg extracts, and $n = 61$ spindles from six egg extracts, respectively, for MeOH, Dent's, MAD, and MAD2), the center line is the mean, the box indicates the 25 to 75% quantiles and the error bars the minimum and maximum values. Average spindle length were MeOH: 31.93 μm ± 7.72, Dent's: 28.57 μm ± 4.26, MAD: 30.62 μm ± 4.99, and MAD2: 31.12 μm ± 4.53 (average value ± SD). Scale bars, 10 μm for unexpanded spindles and 40 μm for expanded spindles. * $p < 0.05$; ** $p < 0.01$; *** $p < 0.001$; *ns*, nonsignificant.

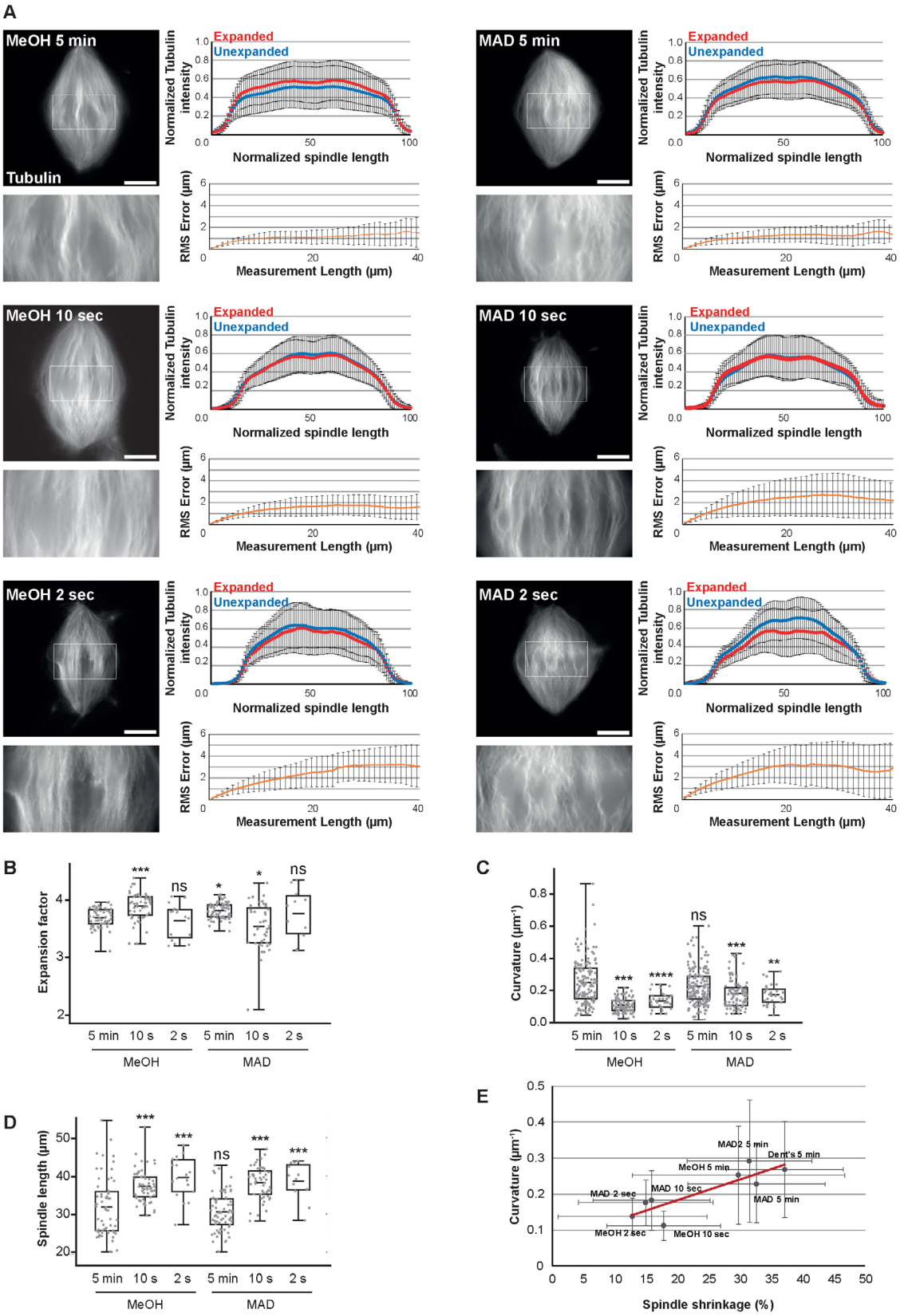


FIGURE 5: Evaluating the effects of decreasing the duration of the postcentrifugation fixation. (A) The six conditions tested on *X. laevis* spindles differing by the composition and duration of the postcentrifugation fixation: MeOH (100% methanol, left), MAD (40% methanol, 40% acetone, and 20% DMSO, right), the durations are indicated on each spindle image. Each top left images show expanded spindles (rhodamine-labeled tubulin signal). Corresponding bottom left images are magnified views of boxed regions in top images. Top right panels are the average normalized fluorescence

Species	Detected area size (μm^2)	Mean number of detected areas (n ± SD)
X. laevis	0.137–0.212 (smallest to single fluorophore)	7.18 ± 6.35
	0.212–0.314 (single microtubule)	215.27 ± 106.65
		Percentage of all detected microtubules: 0.85 ± 0.56%
X. tropicalis	0.128–0.212 (smallest to single fluorophore)	45.07 ± 50.60
	0.212–0.314 (single microtubule)	468.53 ± 270.08
		Percentage of all detected microtubules: 3.40 ± 3.42%

TABLE 1: Detection of single microtubules within *X. laevis* and *X. tropicalis* expanded spindles.

We next compared the distribution of fluorescence intensity, as commonly used (Kitaoka *et al.*, 2018), using a 10-pixel-wide line scan on unexpanded spindles, with a size-corresponding region of interest (ROI) on expanded spindles between the two *Xenopus* species (Supplemental Figure S6E). We observed similar distributions between the two methods with a greater dip in intensities at the *X. tropicalis* spindle center. Conversely, we then analyzed unexpanded spindles with line scans covering the full spindle width, more consistent with our analysis workflow on expanded spindles (Supplemental Figure S6F). Doing so, we observed a generally higher total intensity for *X. laevis*, which was expected given their size differences. Of note, for *X. tropicalis* spindles, which are ∼30% shorter (Brown *et al.*, 2007), the maximum measured intensity in expanded spindles was approximately also 30% lower than for *X. laevis* (60 vs. 90 a.u.). Interestingly, the number of detected bundles in total spindles displayed the same global distributions between the two *Xenopus* species, with a higher number for *X. laevis* (again a difference of about 30% between the two species). The same distributions were observed for the small ROI analysis; however, the counts were higher for *X. tropicalis*, suggesting that microtubules may be denser in these spindles (Supplemental Figure S6, E and F).

Comparing the average number of bundles according to their area between *X. laevis* ($n = 11$ spindles) and *X. tropicalis* ($n = 15$ spindles) revealed that the majority of bundles across the sections were ∼0.5 μm^2 in cross-section area. Considering expanded microtubules as circles of 200 nm in diameter (25 nm for the microtubule plus 25 nm for a cross-linker multiplied by a 4x expansion) to fit in circles of the bundle cross-section area, we estimated that a 0.5 μm^2 bundle cross-sections would correspond to ∼10 microtubules, and 4 μm^2 to ∼100 microtubules. A broader range of bundle sizes was nevertheless observed in *X. laevis* spindles, where it was more restricted to smaller sizes in *X. tropicalis* (Supplemental Figure S6G). Furthermore, we observed a progressive increase in the maximum number of bundles along the spindle, from about 50 bundles in 5% section to 110 in 20%, and 130 in 35%, and decreasing to 110 in 50%. This is consistent with the shape of the spindle and the presence of chromosomes at the spindle center (Supplemental Figure S6G).

Altogether, the linearity between bundle cross-sectional areas and intensities, the correspondence observed between tubulin distributions in unexpanded and expanded spindles, and the coherent distribution of bundle numbers across different spindle sections, confirmed the capacity of our analysis workflow to segment, analyze, and compare microtubule bundle organization between the two *Xenopus* species.

Differently sized microtubule bundles are differentially localized along the spindle length between *X. laevis* and *X. tropicalis*

To analyze the distribution of microtubule bundles in further detail, we summed their areas within each area size bins (Figure 7A).

intensity of tubulin distributions ± SD for unexpanded (blue) and expanded (red) ($n = 57$ spindles from six egg extracts, $n = 51$ spindles from four egg extracts, $n = 17$ from two egg extracts, $n = 64$ spindles from five egg extracts, $n = 45$ spindles from four egg extracts, and $n = 11$ spindles from two egg extracts, respectively, for MeOH 5 min, MeOH 10 s, MeOH 2 s, MAD 5 min, MAD 10 s, and MAD 2 s). Bottom right panels represent the RMS length measurement error as a function of measurement length for pre- versus postexpansion images. The orange line shows the average and the error bars, the SD ($n = 56$ spindles from 6 egg extracts, $n = 52$ spindles from 4 egg extracts, $n = 16$ spindles from two egg extracts, $n = 64$ spindles from 5 egg extracts, $n = 44$ from 4 egg extracts, and $n = 11$ spindles from two egg extracts, respectively, for MeOH 5 min, MeOH 10 s, MeOH 2 s, MAD 5 min, MAD 10 s, and MAD 2 s). (B) Boxplots showing individual spindle expansion factors (same statistics as for RMS error study), the center line is the mean, the box indicates the 25 to 75% quantiles and the error bars the minimum and maximum values. Average expansion factors were MeOH 5 min: 3.68 ± 0.16, MeOH 10 s: 3.88 ± 0.23, MeOH 2 s: 3.63 ± 0.30, MAD 5 min: 3.80 ± 0.14, MAD 10 s: 3.53 ± 0.39, and MAD 2 s: 3.76 ± 0.43 (average value ± SD). (C) Boxplots showing average curvature of microtubules measured by tracking individual microtubule bundles on expanded spindles ($n = 159$ microtubules, $n = 112$ microtubules, $n = 34$ microtubules, $n = 173$ microtubules, $n = 90$ microtubules, and $n = 30$, respectively, for MeOH 5 min, MeOH 10 s, MeOH 2 s, MAD 5 min, MAD 10 s, and MAD 2 s), the center line is the mean, the box indicates the 25 to 75% quantiles and the error bars the minimum and maximum values. Average curvature were MeOH 5 min: 0.25 μm^{-1} ± 0.14, MeOH 10 s: 0.11 μm^{-1} ± 0.04, MeOH 2 s: 0.14 μm^{-1} ± 0.05, MAD 5 min: 0.23 μm^{-1} ± 0.11, MAD 10 s: 0.18 μm^{-1} ± 0.08, MAD 2 s: 0.18 μm^{-1} ± 0.06 (average value ± SD). (D) Boxplots showing individual spindle length measured on unexpanded spindles ($n = 56$ spindles from six egg extracts, $n = 58$ spindles from four egg extracts, $n = 18$ from two egg extracts, $n = 72$ spindles from five egg extracts, $n = 50$ spindles from four egg extracts, and $n = 12$ spindles from two egg extracts, respectively, for MeOH 5 min, MeOH 10 s, MeOH 2 s, MAD 5 min, MAD 10 s, and MAD 2 s), the center line is the mean, the box indicates the 25 to 75% quantiles and the error bars the minimum and maximum values. Average spindle length were MeOH 5 min: 31.93 μm ± 7.72, MeOH 10 s: 37.35 μm ± 4.14, MeOH 2 s: 39.63 μm ± 5.39, MAD 5 min: 30.62 μm ± 5.00, MAD 10 s: 38.24 μm ± 4.25, and MAD 2 s: 38.65 μm ± 4.88 (average value ± SD). (E) Representation of average curvature of microtubules as a function of spindle shrinkage. Black dots, values for indicated conditions, red line, linear trend curve ($R^2 = 0.74$). Scale bars, 40 μm. * $p < 0.05$; ** $p < 0.01$; *** $p < 0.001$; *ns*, nonsignificant.

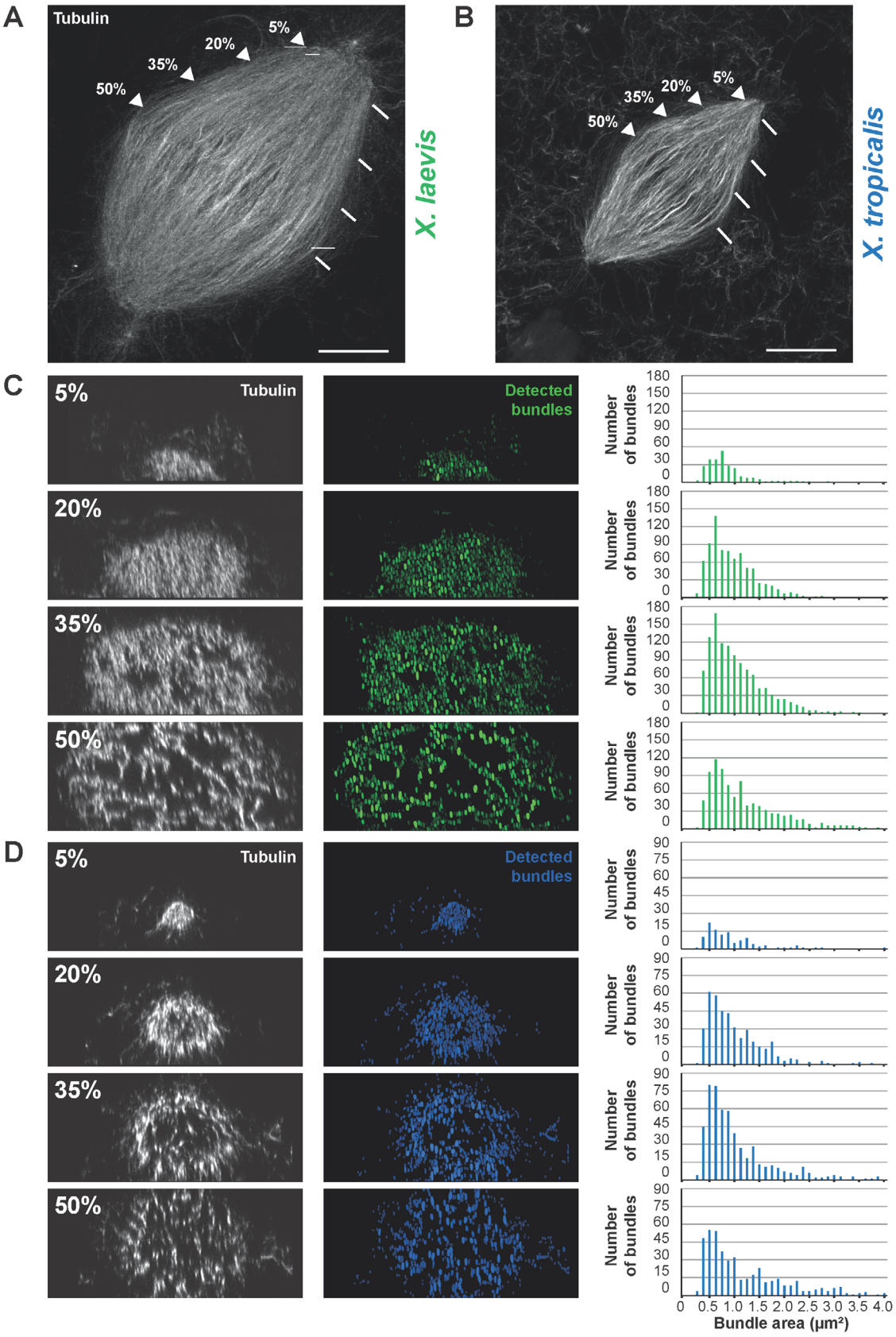


FIGURE 6: Development of an analysis workflow to analyze and compare expanded spindles from *X. laevis* and *X. tropicalis*. (A) Expanded spindle from *X. laevis* egg extract with rhodamine-labeled tubulin signal, imaged with Airyscan microscope, image taken from a 3D rendering in Napari. Arrows and corresponding lines indicate the location of the spindle cross-sections shown in C. (B) Expanded spindle from *X. tropicalis* egg extract with rhodamine-labeled tubulin

First, we examined, for each bundle area bin, their summed area along the length of the spindle and compared them between the two *Xenopus* species. Interestingly, for the smaller bundles (areas of 0.25 and 0.375 μm^2), the total areas they occupied within the entire spindle was greater for *X. tropicalis* than for *X. laevis*. Notably, their prominence was higher in the 35 and 65% sections, with a dip at the spindle center in *X. tropicalis*, while they were mostly homogeneously distributed along the spindles in *X. laevis*. The relative proportions between the two species became equal for the 0.5 μm^2 bundles and were higher for all the larger ones in *X. laevis*. It was also observed that bundles from 0.125 to 0.375 μm^2 for *X. tropicalis* (exemplified with 0.25 and 0.375 μm^2 classes in Figure 7A) and from 0.75 to 1.375 μm^2 for *X. laevis* (exemplified with 1 μm^2 class in Figure 7A) were very strongly represented in the 35 and 65% with a dip at the metaphase plate. However, from 2.0 μm^2 bundles, their distribution shifted to become more represented at the 50% section of both *X. laevis* and *X. tropicalis* spindles, which is even more pronounced for bigger bundles from 3 μm^2 (exemplified with 3 and 4 μm^2 classes in Figure 7A). This suggests that larger bundles, likely the more robust ones, are required at the spindle midzone to ensure spindle bipolarity.

We next generated heatmaps of the total areas of each bundle area classes across the spindle sections to provide a clearer overview and compare the space occupied by the different bundle sizes over the spindle length between *X. laevis* and *X. tropicalis* (Figure 7B). We observed that smaller bundles occupied most of the spindle pole area, and the larger bundles took up more space toward the spindle center. Additionally, it became clearly visible that the global area of *X. tropicalis* spindles were predominantly made up of smaller bundles, while *X. laevis* spindles presented a broader range of bundle sizes.

In a different view, pie charts allowed to us to study partitioning of the differently sized microtubule bundles in each section of the spindle (Figure 7C). In the 5% section, very large (2.0–4.0 μm^2), large (1.0–2.0 μm^2), and small (0.5–1.0 μm^2) bundles were divided in similar proportions between *X. laevis* and *X. tropicalis* (sy) with the main difference being for the very small bundles (0.0–0.5 μm^2), which represented 27% in *X. tropicalis* and only 16% in *X. laevis*. At the 20% section, more than half the section was occupied by large and very large bundles (10 and 43%) in *X. laevis*, whereas this section was divided among very small, small, and large bundles (20, 38, and 32%) in *X. tropicalis*. In the 35% section, the distribution was nearly the same as for the 20% section, except that in both species the proportion of very large bundles nearly doubled. Interestingly, at 50%, there were similar numbers of large bundles and very small bundles in *X. tropicalis* (~20%), whereas in *X. laevis*, although very large bundles also represented 20%, very small bundles accounted for only half of that in *X. tropicalis*. Finally, pie charts combining all sections summarized these observations. In *X. laevis*, large bundles were prominent, followed by small bundles and an equal amount of very large and very small bundles. In *X. tropicalis*, large and small bundles equally shared the majority, followed by very small bundles, which accounted for twice as much as the very large bundles.

To conclude our analysis, we asked whether these observed differences are solely species-specific as a result of evolution to build an optimally sized spindle or if they also respond to size or other spindle parameters. First, we investigated the effect of spindle size and restricted our analysis to spindles with comparable lengths (Supplemental Figure S7A) or widths (Supplemental Figure S7B) between *X. laevis* and *X. tropicalis*. Interestingly, selected *X. laevis* spindles for similar lengths and widths show no obvious difference compared with the whole population. However, *X. tropicalis* spindles selected for comparable lengths seem to show a slight adaptation to increased size by using more very small sized bundles, in particular the tiniest ones (0.25 μm^2), to populate the spindle (Supplemental Figure S7A), which nonetheless still does not resemble the architecture of corresponding *X. laevis* spindles. Although this analysis relied only on few *X. laevis* and *X. tropicalis* spindles with similar lengths within our dataset ($n = 4$ vs. 2), comparing spindles with similar widths with more spindles for both species ($n = 6$ vs. 5), showed the same tendency to a lesser extent (Supplemental Figure S7B). As a correlation between spindle size and width holds between the two species, our results altogether suggest an adaptation of *X. tropicalis* spindles to varying size.

We then questioned the effect of spindle shape, using solidity as a proxy (Supplemental Figure S8A), as well as the amount of chromatin, using DNA volume as a proxy (Supplemental Figure S8B). Strikingly, despite having similar solidity, differences in architecture between *X. laevis* and *X. tropicalis* spindles ($n = 5$ vs. 9) were still distinguishable between the two species and comparable with the whole dataset analysis. However, although selected *X. laevis* spindles for comparable amounts of DNA ($n = 4$) show no obvious difference compared with the whole population, their *X. tropicalis* counterparts ($n = 4$) show an interesting adaptation to the increased amount of DNA. With more DNA, *X. tropicalis* spindles indeed present more and larger sized bundles populating the spindles, while very small bundles (<0.5 μm^2) are pushed away from the DNA. Of note, in this condition, *X. tropicalis* spindles show more similarities with *X. laevis*.

Altogether, these results reveal clear differences in microtubule organization between *X. laevis* and *X. tropicalis*. These differences are likely to be important for building spindles of different sizes while ensuring proper pole stability as well as bipolarity. Though our results are limited by the restricted number of comparable spindles between *X. laevis* and *X. tropicalis*, they point toward the amount of chromatin as a potential important regulator of *X.*

signal, imaged with Airyscan microscope, image taken from a 3D rendering in Napari. Arrows and corresponding lines indicate the location of the spindle cross-sections shown in D. (C) Left images show the tubulin fluorescent signal of cross-sectioned microtubule bundles within respective spindle cross-sections from the *X. laevis* spindle in A (respective spindle sections are indicated in top left corners). Right images show only the detected bundles within each respective spindle cross-sections as detected by the ImageJ macro and color-coded according to their size using Qupath, smaller being darker and larger being brighter. Bar plots (right) show the distribution of these detected bundles, according to their area. (D) Left images show the tubulin fluorescent signal of cross-sectioned microtubule bundles within respective spindle cross-sections from the *X. tropicalis* spindle in B (respective spindle sections are indicated in top left corners). Right images show only the detected bundles within each respective spindle cross-sections in false colors as detected by the ImageJ macro and color-coded according to their size using Qupath, smaller being darker and larger being brighter. Bar plots (right) show the distribution of these detected bundles, according to their area. For C and D, bundle areas are binned into classes of 0.125 μm^2. Each bin is named according to its upper range value. Scale bars, 20 μm.

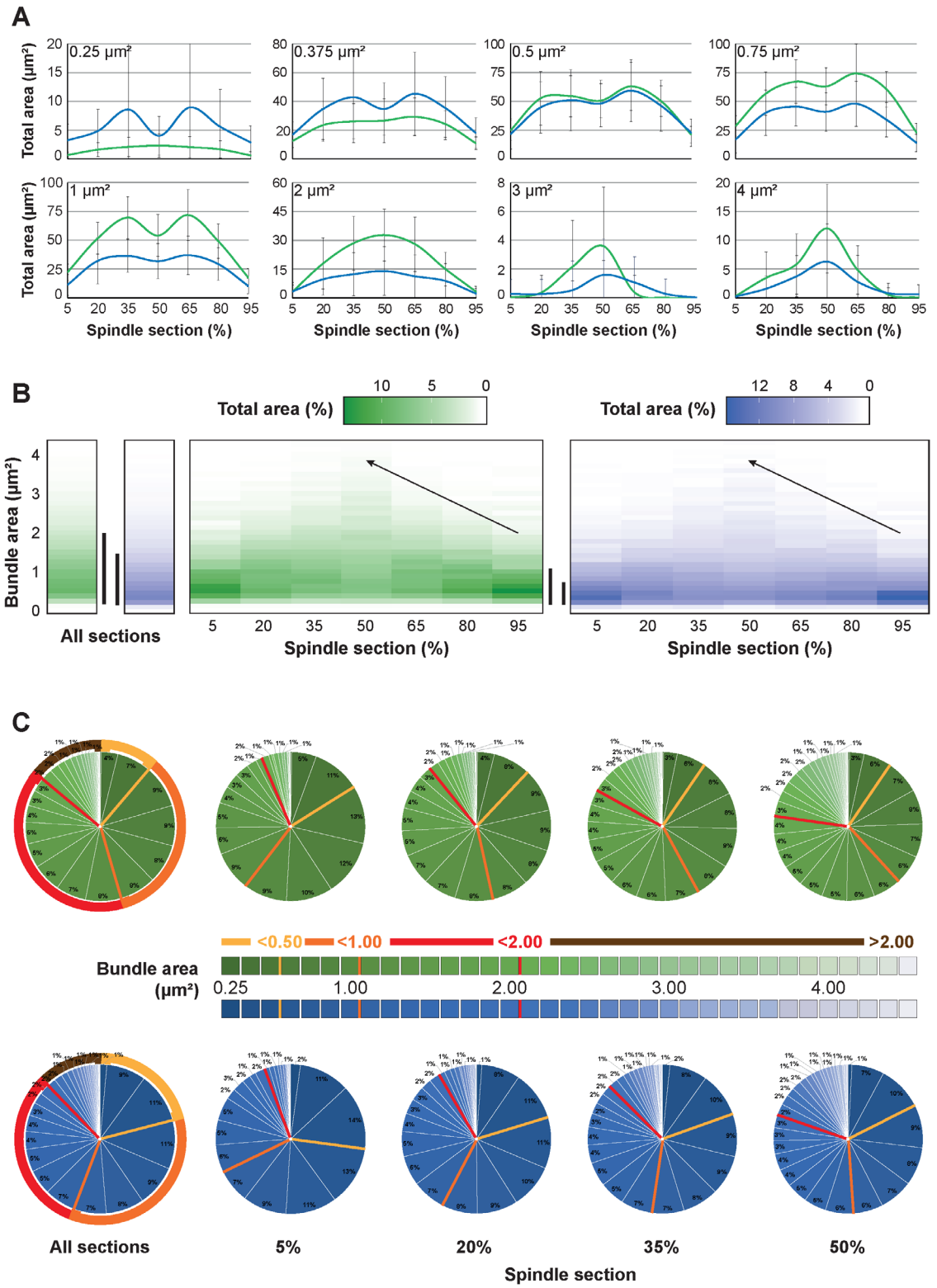


FIGURE 7: Analysis of the organizational differences between spindles from *X. laevis* and *X. tropicalis*. (A) Normalized average total area of indicated bundle area size bins (top left corners) according to the spindle cross-sections from *X. laevis* (green) and *X. tropicalis* (blue). Note that the absence of left–right symmetry for the distributions of large bundles (3 and 4 µm^2) is the results of their low count, see Figure 6. (B) Heatmaps representing for each bundle area size bin (*y*-axis) its normalized average total area (color intensity) for all sections together (left, black lines show the main bundle sizes occupying the entire spindles) and for the different indicated cross-sections of the spindle (*x*-axis) (right, black lines show the main bundle sizes occupying the spindle poles and black arrows indicate the increase in bundle sizes as approaching the spindle center) from *X. laevis* (green) and *X. tropicalis* (blue). (C) Pie charts of normalized average total area of bundles according to their binned areas for all sections together (left pie charts) and for the different indicated

tropicalis spindle architecture, as well as spindle size to a much lesser extent. Further investigation will be necessary to link our observations to the underlying mechanisms that generate distinct spindle architectures.

DISCUSSION

Electron microscopy techniques can achieve single microtubule resolution, but analyzing entire *Xenopus* spindles remains out of reach due to their large size. Meanwhile, the high microtubule density in these spindles, together with the low resolution of traditional fluorescence microscopy, makes it challenging to accurately study their organization beyond global spindle architecture. As a result, our understanding of microtubule arrangement within *Xenopus* spindles has remained largely speculative. In this study, we developed an optimized, simple and versatile ExM protocol, coupled with a specifically developed analysis workflow, to address this knowledge gap and compare *X. laevis* and *X. tropicalis* spindles.

Using our analysis workflow, we could reproduce previous observations that tubulin fluorescence intensity is higher at the poles and reduced in the center of the *X. tropicalis* spindles, whereas *X. laevis* spindles exhibit more uniform tubulin distribution (Kitaoka *et al.*, 2018) (Supplemental Figure S6, C and D). Yet, our detailed analysis revealed distinct microtubule arrangements and variations in spindle architecture that were not detectable with earlier imaging methods. We found that *X. laevis* spindles exhibit a broader range of bundle sizes, while *X. tropicalis* spindles are more limited to smaller bundles (Figures 6E and 7B), with ∼30% fewer bundles overall. This suggests that *X. tropicalis* could compensate for its fewer microtubules by maintaining smaller bundle sizes while increasing bundle density (Supplemental Figure S6, C and D). Additionally, we observed that both species favor larger bundle sizes (3–4.5 μm^2 classes) near and at the spindle center, but *X. tropicalis* spindles prefer very small bundles (0.125–0.375 μm^2), while *X. laevis* spindles favor medium-sized bundles (0.75–1.375 μm^2) to populate the spindle between the poles and the mid-zone (Figure 7A). This suggests that spindle architecture is regulated to optimize bundle size, which could be crucial for maintaining spindle integrity in smaller spindles, while ensuring chromosome attachment and bipolarity with less flexible bundle sizes. Notably, if the large bundles at the spindle center, of the same sizes between *X. laevis* and *X. tropicalis*, were in part kinetochore fibers, this could explain why kinetochore fibers would need to be specifically differentially regulated by katanin between these two species to maintain spindle integrity in the context of differentially sized spindles (Loughlin *et al.*, 2011). Thanks to the immunolabeling possibilities offered by our protocol, further studies would allow labeling of kinetochore proteins to determine which of these bundles are kinetochore fibers and if these are different from other bundles. Moreover, investigating the contribution of length and width, we found that *X. tropicalis* spindles seem to modify their architecture to handle an increase in size, while *X. laevis* spindle architecture is not modified for smaller sizes. This suggests that either *X. tropicalis* spindle architecture is less flexible to changes in size or that it is more complex to cope with an increase in size than a decrease. Previous studies reported, using chromatin-coated beads with a controlled quantity of DNA per bead, that chromatin mass influences in a direct manner the size of the spindle, but only marginally with a size increase of only 10% despite a 400% increase in the amount of DNA (Dinarina *et al.*, 2009). However, although the size change is marginal, it remained unknown how DNA amount affected spindle architecture. In fact, our results suggest that additional chromatin promotes more and larger bundles in *X. tropicalis* spindles. One possibility is that the increased volume occupied by the chromosomes forces the spindle to adjust its architecture to the physical constraint. Another possibility is that this could be due to more chromatin-driven microtubule nucleation. Taken together, these data offer new insights to better understanding of how spindle architecture adapts to different morphologies and constraints but fully understanding the contribution of both size and DNA amount, and the underlying mechanisms, will require further analyses.

In developing this protocol, we made several important technical observations. First, rather than relying on an existing protocol, we reevaluated several steps of classical expansion protocols. This was motivated by the fact that even within the same cell, different cellular organelles can exhibit varying expansion factors (Büttner *et al.*, 2021). Additionally, the development of a holed metal slide to image the same spindles before and after expansion proved to be key. This allowed us to calculate the local expansion factor for each spindle rather than relying on the global gel expansion (Truckenbrodt *et al.*, 2019), and systematically assess the quality of expansion under different conditions. Notably, we found that the most critical step was actually sample fixation. Both aldehyde fixatives and dehydration fixation can introduce artifacts (Cross and Williams Jr., 1991; Melan, 1999). We observed that fixation causes spindle shrinkage and correlates with wavy microtubules (Figure 5E). In addition, overfixation led to poor incorporation of structures into the gel and disturbed expansion (Supplemental Figure S4D), while underfixation caused spindles to disappear between pre- and postexpansion imaging, likely because they washed off during processing. We also aimed to preserve the rhodamine-labeled tubulin signal and adequately fix the sample onto the coverslip for preexpansion immunolabeling (Supplemental Figure S5). It is therefore only by carefully and systematically evaluating the different parameters and the resulting expansion quality, and finding the proper balance that we were able to develop this optimized protocol.

Through this study, we established a simple ExM protocol optimized for the *Xenopus* egg extract system. This protocol provided new insights into spindle architecture adaptation and will facilitate further high-resolution studies of spindle components, such as molecular motors or kinetochores, for instance, or other microtubule structures, such as asters, as well as spindles from other *Xenopus* species (Kitaoka *et al.*, 2018; Miller *et al.*, 2019).

MATERIALS AND METHODS

Request a protocol through *Bio-protocol*

Animals

All animal experimentation in this study was performed according to our animal use protocol APAFiS #26858-2020072110205978 approved by the Animal Use Ethic Committee (#7, Rennes, France) and the French Ministry of Higher Education, Research and

cross-sections of the spindle or (right pie charts) from *X. laevis* (green) and *X. tropicalis* (blue). Colored bars in pie charts delimit areas of greater classes of bundle areas (bin 0.0 – 0.5 μm^2, yellow; bin 0.625 – 1.0 μm^2, orange; bin 1.125 – 2.0 μm^2, red; >2.0 μm^2, brown, as depicted on the left pie chart). For A to C, bundle areas are binned into classes of 0.125 μm^2. Each bin is named according to its upper range value; $n =$ 11 spindles from three egg extracts, $n = 15$ spindles from three egg extracts, respectively, for *X. laevis* and *X. tropicalis*.

Innovation. Mature *X. laevis* and *X. tropicalis* female frogs were ovulated with no harm to the animals with rest intervals between ovulations of at least a 6- and 3-mo, respectively.

Chemicals

Unless otherwise stated, all chemicals were purchased from Sigma-Aldrich, Merck.

Xenopus egg extracts

X. laevis and *X. tropicalis* egg extracts were prepared and cycled spindle reactions conducted as described previously (Maresca and Heald, 2006; Kitaoka *et al.*, 2024). Briefly, eggs arrested in metaphase of meiosis II were collected, dejellied, and fractionated by centrifugation. The cytoplasmic layer was isolated, supplemented with 10 µg/ml (final) of each leupeptin, pepstatin, and chymostatin protease inhibitors, 20 µg/ml (final) of cytochalasin B, a creatine phosphate and ATP energy regeneration mix, as well as 400 nM (final) rhodamine-labeled porcine brain tubulin (Cytoskeleton). Then, cycled spindle reactions containing 25 µl of cytostatic factor–arrested (CSF) extract from *X. laevis* or *X. tropicalis* were supplemented with 400 µM Ca2+ and incubated for 5.5 min at 23°C to bring the extract into interphase. Resulting interphasic extract was supplemented with *X. laevis* or *X. tropicalis* sperm nuclei, prepared as previously published (Hazel and Gatlin, 2018), at a final concentration of 500 to 1000 per µL. After about 45 min (30 min for *X. tropicalis*), the DNA was replicated and 50% of fresh CSF extract was added to the reaction leading to cycle the extract back to metaphase, which then produced bipolar spindles around 45 min after adding back at 23°C.

Spindle spin-down

When organized bipolar spindles were observed, the ~50 µl reactions were mixed to 1 ml of dilution solution containing 30% glycerol, 1X BRB80 (BRB80 5X: 400 mM 1,4-pipperazinediethanesulfonic acid, 5 mM $MgCl_2$, 5 mM EGTA, pH 6.8), 0.5% Triton X-100 and supplemented with 2.5 or 5% formaldehyde or 0.05, 0.10, 0.15 or 0.25% glutaraldehyde (Electron Microscopy Science), or no fixative and layered over a 5 ml cushion containing 40% glycerol in 1X BRB80. The reactions were then spun onto coverslips centrifuged at 17,000 × *g* for 15 min or 6000 × *g* for 20 min at 16°C. After that, the samples were fixed on the coverslips by putting them in −20°C methanol, Dent's (methanol/DMSO, 4:1), MAD (methanol/acetone/DMSO, 2:2:1) or MAD2 (methanol/acetone/DMSO, 3:1:1) baths for 2 s to 5 min depending on the protocol. Coverslips were then put on parafilm with the sample facing up in a large petri dish kept humid with wet kimwipes and washed trice with PBS supplemented with 0.1% (vol/vol) IGEPAL CA-630 (PBSI) to stop dehydration and rehydrate the samples and then twice with PBS. Coverslips were finally processed either for pregelation immunofluorescence, preexpansion imaging or directly for anchoring.

Analysis of unfixed spindles

To image live spindles, imaging chambers were prepared as described previously (Field and Mitchison, 2018). Briefly, coverslips (18 and 22 mm, square) were passivated using PLL-g-PEG (SuSoS, Dübendorf, Switzerland), the 22-mm coverslip was attached to a metal support slide, passivated-face up, using VALAP (vaseline:lanolin:paraffin, 1:1:1), 7.5 µl of egg extract spindle reaction was pipetted onto the coverslip, and the 18-mm coverslip was immediately placed on top, passivated-face down. The chamber was finally sealed using VALAP.

Alternatively, spindle reactions were processed for spin-down as detailed above but without fixative in the dilution buffer or any postcentrifugation fixation. After spin-down, the coverslips were directly retrieved, mounted on a slide using VectaShield (Vector-Labs), and sealed using nail polish.

In both cases, the spindles were subsequently imaged following the same procedure as described below for postexpansion imaging using Airyscan.

Preexpansion imaging

For preexpansion imaging, coverslips were first incubated for 5 min with PBS containing 10 µg/ml Hoechst 33342 and rinsed twice with PBS. Coverslips were then mounted on the cavity of a homemade metal slide filled with PBS. Imaging was performed on an Olympus BX51 microscope equipped with a Lumencor SOLA SE U-nIR light source, and a Photometrics Prime-BSI sCMOS Back Illuminated camera. Images were acquired using the µManager acquisition software v1.4 (Edelstein *et al.*, 2014). After imaging, an excess of PBS was added into the cavity of the metal slide to retrieve the coverslip and replace it on the parafilm of the humid petri dish shielded from light and recovered with PBS.

Sample anchoring and gelation

The PBS was removed, the coverslips were rinsed once with 120 µl of anchoring solution (0.1 mg/ml 6-((acryloyl) amino) hexanoic acid, succinimidyl ester (AcX,SE; Thermo Fisher Scientific)), and incubated in 120 µl of fresh anchoring solution for 1 h at room temperature and then processed for gelation. A drop of 75 µl of ExM gelation mix (Chen *et al.*, 2015; Tillberg *et al.*, 2016) (8.625% [wt/wt] sodium acrylate, 2.5% [wt/wt] acrylamide, 0.15% [wt/wt; Interchim] N,N′-methylenebisacrylamide, 2 M NaCl in 1X PBS) or U-ExM gelation mix (Gambarotto *et al.*, 2018) (19% [wt/wt] sodium acrylate, 10% [wt/wt] acrylamide, 0.1% [wt/wt] N,N′-methylenebisacrylamide in 1X PBS) supplemented with 0.2% TEMED and then 0.2% ammonium persulfate was placed on the parafilm. After aspiring all the anchoring solution, the coverslips were rapidly but carefully put on the drop with the spindles facing the gelation solution. After 10 min of polymerization at room temperature, the wet kimwipes were removed and the reaction was then left to polymerized for 30 min at 37°C in the petri dish shielded from light.

Digestion or denaturation of samples in the gels

For the digestion procedure, the coverslips and their attached gel were transferred in a small glass petri dish containing the digestion buffer (1X TAE, 0.5% Triton X-100, 0.8M guanidine hydrochloride). Coverslips were gently removed from the gel with a spatula and the buffer was supplemented with proteinase K (New England Biolabs) at 8 U/mL at the last moment. The digestion was performed at 37°C for 1 h. Gels were then collected with the spatula and put in new small petri dish, washed three times for 5 min in PBS supplemented with 0.1% Triton X-100 (PBT), twice in PBS, and processed for expansion.

For the denaturation procedure, the coverslips and their attached gel were transferred in a small glass petri dish and incubated for 15 min at room temperature in denaturation buffer (200 mM SDS, 200 mM NaCl and 50 mM Tris [Euromedex], pH 9). Coverslips were then gently removed from the gel with a spatula and gels were incubated in fresh denaturation buffer for 30 min in a water bath at 95°C. Following denaturation, the gels were washed three times for 5 min in PBT, twice in PBS and processed either for postgelation immunofluorescence or expansion.

Expansion

Gels, in glass petri dish, were first incubated for 5 min at room temperature with 1 ml of the Hoechst solution diluted in PBS. Following three washes with PBS, MilliQ water was added and left for 1 h. Gels were further expanded by changing for fresh MilliQ water and left for at least 30 min before imaging. After imaging, gels were put back into 1X PBS, rinsed once and stored at 4°C shielded from light to preserve the fluorescent signal.

Postexpansion imaging

To compare the same spindles before and after expansion, the whole gel was mounted on two microscope slides taped together. The entire gel can then be screened, keeping its integrity and allowing to retrieve all structures of interest. To mount the gel, the milliQ water was removed, the gel taken out and put on a kimwipe to dry it. The gel was then transferred to the double slide and covered with two large (24×60) coverslips to be imaged on the Olympus BX51 microscope as for preexpansion imaging.

For greater resolution imaging, a Zeiss LSM 880 confocal microscope with Airyscan was used. Expanded gels were cut into small pieces to be mounted on a glass bottom dish (MatTek) coated with poly-L-lysine to prevent gel drifting during imaging. For a better gel adhesion to the glass, gel pieces were dried on kimwipes before mounting. The inverted Zeiss Axio Observer 7 microscope equipped with Confocal Scan Head LSM 880 and Airyscan detector was used in Fast-Airyscan mode and images were acquired using a 40x/1.2 W C Apochromat objective with powers of 20 and 30% for the 561 and 405 nm lasers, respectively, and spacing of 0.25 µm in Z. Images are mean averages of two scans with a depth of 16 bits. Channels were acquired sequentially, and pinhole size was always chosen to correspond to 1 airy unit.

Optional pregelation immunofluorescence

For our proof of principle, coverslips were first blocked with PBS supplemented with 3% BSA (Euromedex) (PBS-BSA) overnight at 4°C in a large humid petri dish. On the next morning, each coverslip was washed with PBS–BSA. Then 110 µl of PBS–BSA containing 1:250 of antidynein mouse antibody (Invitrogen, #14-9772-80) was put on each coverslip for 1 h at room temperature in the large humid petri dish. Coverslips were then washed with PBSI 3 times for 5 min and subsequently incubated for 30 min at room temperature with 110 µl of PBSI containing 1:500 of goat anti-mouse AlexaFluor488-coupled antibody (Invitrogen, # A-11029) in the large humid petri dish shielded from light. Coverslips were washed in PBSI three times for 5 min and then incubated for 5 min at room temperature with 110 µl of the Hoechst solution diluted in PBSI. Coverslips were washed in PBSI 3 times for 5 min and twice with PBS. Coverslips were then processed either for preexpansion imaging and anchoring. This pregelation immunofluorescence option is important for antibodies, like the antidynein, that are not suitable for postexpansion immunofluorescence in our hands (i.e., anti-Eg5 Novusbio #NB500-181, anti-p150 DB Biosciences #610473, anti–γ-tubulin Sigma-Aldrich #T6557, anti-chTOG Abcam #AB86073). Of note, we found the anti–α-tubulin Sigma-Aldrich #T6199 and the anti-polyglutamate chain (polyE) AdipoGene Life Sciences #AG-25B-0030 to be suitable for postexpansion immunofluorescence.

Analysis of spindle parameters

Length and normalized intensity distribution profile were measured for spindles. For each spindle length, a line with a width of 10 pixels for unexpended and 40 pixels for expanded spindles was drown from one pole to another in Fiji (Schindelin *et al.*, 2012). Intensity line scans measured from pole-to-pole were then normalized to 100% of the length of each spindle using an automated Java ImageJ plugin developed by Dr. Xiao Zhou (https://github.com/XiaoMutt/AiSpindle), to account for size differences between spindles pre- versus postexpansion. The intensities were then also normalized to the maximum intensity of each dataset to account for the overall dimmer rhodamine signal after expansion, resulting from the fluorophore dilution, by the third power of the expansion factor, inherent to ExM. To compare tubulin distribution between pre- versus postexpansion, the same spindles were systematically analyzed in the same order and with the line carefully placed at the same location and in the same orientation.

Expansion factors and distortions were measured using Elastix (http://elastix.isi.uu.nl) and a Mathematica (Wolfram) script as described previously (Chozinski *et al.*, 2016). Briefly, postexpansion images were aligned with corresponding preexpansion images using linear transformations (rotation, scaling, and translation). The linearly transformed postexpansion images were then nonlinearly deformed to match the preexpansion images. Quantitative comparison of the linearly and nonlinearly transformed postexpansion images produced values for RMS deviation over a range of length scales. Each RMS plot was generated with one set of representative pre- and postexpansion images.

Curvature measures were performed on Fiji using Kappa plugin (Mary and Brouhard, 2019) following microtubule bundles from pole-to-pole on expanded spindles.

Expanded spindle microtubule bundle analysis workflow

As shown in Supplemental Figure S1, the analysis workflow consists of the manual selection of coordinates of the two microtubule spindle poles to take out spindle cross-sections for microtubule bundle quantification as well as the three-dimensional (3D) segmentation of the spindle and DNA volumes.

Spindle poles selection. To ensure the accurate localization of the two spindle poles, these two reference points are manually defined by the user.

First registration. From the spindle pole coordinates, a translation in the *xy* plane is first applied to position the spindle center at the image center and a rotation around *z*-axis is performed to align the spindle axis with the *x*-axis. The image volume is then transformed to show z resolution in all three dimensions, allowing segmentations to be fully achieved in 3D with a reasonable management of RAM memory. All those transformations are performed with the CLIJ suite plugin (Haase *et al.*, 2020a, 2020b) that takes advantage of GPU computational power for a fast implementation. This reorientation of the spindles allows its subsequent sectioning for analysis.

Getting rid of intensities coming from other spindles. As other spindles might be close and acquired in the same image, it is possible to define the spindle and/or DNA area with a polyline ROI to exclude intensity coming from outside the spindle of interest.

Microtubule bundle quantification. A rotation around the *y*-axis is applied to align the spindle axis along the *z*-axis with the TransformJ plugin (Meijering *et al.*, 2001), followed by an interpolation to get back to original *xy* resolution for spindle cross-sections. Microtubule bundles at selected cross-sections (possible from 5 to 95%, every 5%) are segmented with the deep learning approach

Stardist (Schmidt *et al.*, 2018). Although Stardist was designed for nuclei segmentation, the available pretrained models did surprisingly okay on segmenting the bundles but did not show a sufficient accuracy performance. A new model was therefore trained on 10 images showing cross-sections of microtubules, of which 3162 were manually annotated, 2 images were used for validation. For training, images were normalized with a 1–99.8 quantile. The new model was initialized with the versatile fluorescence model and trained for 1000 epochs. The trained model was converted as a TF_Saved model to be used in the Stardist Fiji plugin.

Whole-spindle segmentation. The image stack for microtubule channel is filtered with a Gaussian blur and thresholded with the Huang method (Huang and Wang, 1995). All components with an area inferior to a minimum area for the spindle equal to 1000 pixels in this study are filtered out. The convex shape of the spindle is computed with the MorpholibJ plugin (Legland *et al.*, 2016).

DNA segmentation. Eight-image stacks were used to train a voxel classifier with LABKIT (Arzt *et al.*, 2022), which allows then to segment DNA from any image stack. All components with an area inferior to a minimum area for the DNA region equal to 100 pixels in this study are filtered out.

Measurements and result visualization. A list of measurements (centroid coordinates, area, perimeter, ellipse fitting, average intensity, and total intensity) is exported for each bundle and combined in an Excel file with the Excel function plugin. At each selected cross-section, the image of bundles and the segmentations displayed as outlines is generated to visually inspect the results. The volumes of the spindle, its convex shape and DNA as well as the coordinates of the spindle poles are exported in the same Excel file. The segmented volumes for the spindle, its convex shape as well as the segmented DNA are also exported for visual inspection. Finally, all parameters are defined in a .csv file for reproducibility.

Code. The workflow was coded as an ImageJ (Schneider *et al.*, 2012) macro and is available at https://github.com/tpecot/IJmacro_MicrotubuleBundlesQuantification/blob/main/quantification.ijm". The Stardist model trained to segment bundles of microtubules is available at "https://github.com/tpecot/IJmacro_MicrotubuleBundlesQuantification/blob/main/TF_SavedModel.zip". The voxel classifier trained to segment DNA is available at "https://github.com/tpecot/IJmacro_MicrotubuleBundlesQuantification/blob/main/DNA_pixelClassifier.classifier".

Image visualization, data compilation, and statistics

Image stacks were visualized in Fiji (ImageJ 1.54f) and in Napari (version 0.4.19; napari.org) and processed in Fiji. Data were analyzed and statistics performed using Excel (Microsoft), Mathematica (Wolfram), and the R suite (www.r-project.org). Averages and standard deviations were calculated. One-way ANOVA with post hoc Dunett's test were performed to test for statistical significance.

ACKNOWLEDGMENTS

We thank the members of the Gibeaux and the Heald labs for their support. We thank the members of the FAIIA and MRic facilities, in particular Dr. Xavier Pinson. We are grateful to Paul Guichard and Virginie Hamel for guidance in developing this protocol as well as Julien Maurais for taking great care of our frogs. G.G. was supported by PhD fellowships from the Region Bretagne (ARED) and from the Fondation pour la Recherche Médicale (FRM) FDT202304016369, and M.K. by a National Science Foundation (NSF) GRFP fellowship. R.H. was supported by NIH MIRA grant R35 GM118183 and the Flora Lamson Hewlett Chair, and R.G. by a Human Frontier Science Program grant CDA00019/2019-C.

REFERENCES

Arzt M, Deschamps J, Schmied C, Pietzsch T, Schmidt D, Tomancak P, Haase R, Jug F (2022). LABKIT: Labeling and segmentation toolkit for big image data. Front Comput Sci 4, 777728.

Balzarotti F, Eilers Y, Gwosch KC, Gynnå AH, Westphal V, Stefani FD, Elf J, Hell SW (2017). Nanometer resolution imaging and tracking of fluorescent molecules with minimal photon fluxes. Science 355, 606–612.

Brown KS, Blower MD, Maresca TJ, Grammer TC, Harland RM, Heald R (2007). Xenopus tropicalis egg extracts provide insight into scaling of the mitotic spindle. J Cell Biol 176, 765–770.

Büttner M, Lagerholm CB, Waithe D, Galiani S, Schliebs W, Erdmann R, Eggeling C, Reglinski K (2021). Challenges of using expansion microscopy for super-resolved imaging of cellular organelles. ChemBioChem 22, 686–693.

Chen F, Tillberg PW, Boyden ES (2015). Expansion microscopy. Science 347, 543–548.

Chen F, Wassie AT, Cote AJ, Sinha A, Alon S, Asano S, Daugharthy ER, Chang JB, Marblestone A, Church GM, *et al.* (2016). Nanoscale imaging of RNA with expansion microscopy. Nat Methods 138, 679–684.

Chozinski TJ, Halpern AR, Okawa H, Kim HJ, Tremel GJ, Wong ROL, Vaughan JC (2016). Expansion microscopy with conventional antibodies and fluorescent proteins. Nat Methods 13, 485–488.

Chunduri NK, Storchová Z (2019). The diverse consequences of aneuploidy. Nat Cell Biol 21, 54–62.

Cross AR, Williams RCJr., (1991). Kinky microtubules: Bending and breaking induced by fixation in vitro with glutaraldehyde and formaldehyde. Cell Motil 20, 272–278.

Crowder ME, Strzelecka M, Wilbur JD, Good MC, Von Dassow G, Heald R (2015). A comparative analysis of spindle morphometrics across metazoans. Curr Biol 25, 1542–1550.

Dent JA, Polson AG, Klymkowsky MW (1989). A whole-mount immunocytochemical analysis of the expression of the intermediate filament protein vimentin in Xenopus. Development 105, 61–74.

Dinarina A, Pugieux C, Corral MM, Loose M, Spatz J, Karsenti E, Nédélec F (2009). Chromatin shapes the mitotic spindle Cell 138, 502–513.

Edelstein AD, Tsuchida MA, Amodaj N, Pinkard H, Vale RD, Stuurman N (2014). Advanced methods of microscope control using μManager software. J Biol Methods 1, e10.

Field CM, Mitchison TJ (2018). Assembly of spindles and asters in *Xenopus* egg extracts. Cold Spring Harb Protoc pdb.prot099796.

Gambarotto D, Zwettler FU, Le Guennec M, Schmidt-Cernohorska M, Fortun D, Borgers S, Heine J, Schloetel JG, Reuss M, Unser M, *et al.* (2018). Imaging cellular ultrastructures using expansion microscopy (U-ExM). Nat Methods 161, 71–74.

Geisterfer ZM, Guilloux G, Gatlin JC, Gibeaux R (2021). The cytoskeleton and its roles in self-organization phenomena: Insights from *Xenopus* egg extracts. Cells 10, 2197.

Gibeaux R, Acker R, Kitaoka M, Georgiou G, van Kruijsbergen I, Ford B, Marcotte EM, Nomura DK, Kwon T, Veenstra GJC, *et al.* (2018). Paternal chromosome loss and metabolic crisis contribute to hybrid inviability in *Xenopus*. Nature 553, 337–341.

Gibeaux R, Lang C, Politi AZ, Jaspersen SL, Philippsen P, Antony C (2012). Electron tomography of the microtubule cytoskeleton in multinucleated hyphae of *Ashbya gossypii*. J Cell Sci 125, 5830–5839.

Götz R, Panzer S, Trinks N, Eilts J, Wagener J, Turrà D, Di Pietro A, Sauer M, Terpitz U (2020). Expansion microscopy for cell biology analysis in fungi. Front Microbiol 11, 574.

Guilloux G, Gibeaux R (2020). Mechanisms of spindle assembly and size control. Biol Cell 112, 369–382.

Haase R, Jain A, Rigaud S, Vorkel D, Rajasekhar P, Suckert T, Lambert TJ, Nunez-Iglesias J, Poole DP, Tomancak P, *et al.* (2020a). Interactive design of GPU-accelerated image data flow graphs and cross-platform deployment using multi-lingual code generation. bioRxiv, 2020.11.19.386565.

Haase R, Royer LA, Steinbach P, Schmidt D, Dibrov A, Schmidt U, Weigert M, Maghelli N, Tomancak P, Jug F, *et al.* (2020b). CLIJ: GPU-accelerated image processing for everyone. Nat Methods 17, 5–6.

Hannak E, Heald R (2006). Investigating mitotic spindle assembly and function in vitro using *Xenopus* laevis egg extracts. Nat Protoc 1, 2305–2314.
Hazel JW, Gatlin JC (2018). Isolation and demembranation of *Xenopus* sperm nuclei. Cold Spring Harb Protoc pdb.prot099044.
Heiligenstein X (2011). Electron microscopy and new technological approaches to investigate structural elements of the mitotic apparatus in *Saccharomyces cerevisiae* and *Xenopus laevis*. Available from: https://archiv.ub.uni-heidelberg.de/volltextserver/12932/. Accessed July 3, 2024.
Helmke KJ, Heald R (2014). TPX2 levels modulate meiotic spindle size and architecture in *Xenopus* egg extracts. J Cell Biol 206, 385–393.
Helmke KJ, Heald R, Wilbur JD (2013). Interplay between spindle architecture and function. Int Rev Cell Mol Biol 306, 83–125.
Hirst WG, Biswas A, Mahalingan KK, Reber S (2020). Differences in intrinsic tubulin dynamic properties contribute to spindle length control in *Xenopus* species. Curr Biol 30, 2184–2190.e5
Höög JL, Schwartz C, Noon AT, O'Toole ET, Mastronarde DN, McIntosh JR, Antony C (2007). Organization of interphase microtubules in fission yeast analyzed by electron tomography. Dev Cell 12, 349–361.
Huang L-K, Wang M-JJ (1995). Image thresholding by minimizing the measures of fuzziness. Pattern Recognit 28, 41–51.
Jiang N, Kim HJ, Chozinski TJ, Azpurua JE, Eaton BA, Vaughan JC, Parrish JZ (2018). Superresolution imaging of *Drosophila* tissues using expansion microscopy. Mol Biol Cell 29, 1413–1421.
Kao P, Nodine MD (2019). Transcriptional activation of Arabidopsis zygotes is required for initial cell divisions. Sci Rep 9, 17159.
Kiewisz R, Fabig G, Conway W, Baum D, Needleman D, Müller-Reichert T (2022). Three-dimensional structure of kinetochore-fibers in human mitotic spindles. Elife 11, e75459.
Kitaoka M, Guilloux G, Heald R, Gibeaux R (2024). Preparation of *Xenopus* borealis and *Xenopus* tropicalis egg extracts for comparative cell biology and evolutionary studies. Methods Mol Biol 2740, 169–185.
Kitaoka M, Heald R, Gibeaux R (2018). Spindle assembly in egg extracts of the Marsabit clawed frog, *Xenopus borealis*. Cytoskeleton 75, 244–257.
Ku T, Swaney J, Park J-Y, Albanese A, Murray E, Cho JH, Park Y-G, Mangena V, Chen J, Chung K (2016). Multiplexed and scalable super-resolution imaging of three-dimensional protein localization in size-adjustable tissues. Nat Biotechnol 34, 973–981.
Legland D, Arganda-Carreras I, Andrey P (2016). MorphoLibJ: Integrated library and plugins for mathematical morphology with ImageJ. Bioinformatics 32, 3532–3534.
Lohka MJ, Masui Y (1983). Formation in vitro of sperm pronuclei and mitotic chromosomes induced by amphibian ooplasmic components. Science 220, 719–721.
Loughlin R, Wilbur JD, McNally FJ, Nédélec FJ, Heald R (2011). Katanin contributes to interspecies spindle length scaling in xenopus. Cell 147, 1397–1407.
Maresca TJ, Heald R (2006). Methods for studying spindle assembly and chromosome condensation in *Xenopus* egg extracts. Methods Mol Biol 322, 459–474.
Mary H, Brouhard GJ (2019). Kappa (κ): Analysis of curvature in biological image data using B-splines. bioRxiv.
Meijering EHW, Niessen WJ, Viergever MA (2001). Quantitative evaluation of convolution-based methods for medical image interpolation. Med Image Anal 5, 111–126.
Melan MA (1999). Overview of cell fixatives and cell membrane permeants. Methods Mol Biol 115, 45–56.
Miller KE, Session AM, Heald R (2019). Kif2a scales meiotic spindle size in *Hymenochirus boettgeri*. Curr Biol 29, 3720–3727.e5.
Park H-E, Choi D, Park JS, Sim C, Park S, Kang S, Yim H, Lee M, Kim J, Pac J, *et al.* (2019). Scalable and isotropic expansion of tissues with simply tunable expansion ratio. Adv Sci 6, 1901673.
Redemann S, Baumgart J, Lindow N, Shelley M, Nazockdast E, Kratz A, Prohaska S, Brugués J, Fürthauer S, Müller-Reichert T (2017). *C. elegans* chromosomes connect to centrosomes by anchoring into the spindle network. Nat Commun 8, 15288.
Sahl SJ, Hell SW, Jakobs S (2017). Fluorescence nanoscopy in cell biology. Nat Rev Mol Cell Biol 18, 685–701.
Sauer G, Körner R, Hanisch A, Ries A, Nigg EA, Silljé HHW (2005). Proteome analysis of the human mitotic spindle. Mol Cell Proteomics 4, 35–43.
Schindelin J, Arganda-Carreras I, Frise E, Kaynig V, Longair M, Pietzsch T, Preibisch S, Rueden C, Saalfeld S, Schmid B, *et al.* (2012). Fiji: An open-source platform for biological-image analysis. Nat Methods 9, 676–682.
Schmidt U, Weigert M, Broaddus C, Myers G (2018). Cell detection with star-convex polygons. In: Medical Image Computing and Computer Assisted Intervention – MICCAI 2018, ed. AF Frangi, JA Schnabel, C Davatzikos, C Alberola-López, and G Fichtinger, Cham: Springer International Publishing, 265–273.
Schneider CA, Rasband WS, Eliceiri KW (2012). NIH image to ImageJ: 25 years of image analysis. Nat Methods 9, 671–675.
Sun De, Fan X, Shi Y, Zhang H, Huang Z, Cheng B, Tang Q, Li W, Zhu Y, Bai J, *et al.* (2020). Click-ExM enables expansion microscopy for all biomolecules. Nat Methods 181, 107–113.
Tillberg PW, Chen F, Piatkevich KD, Zhao Y, Yu CC, English BP, Gao L, Martorell A, Suk HJ, Yoshida F, *et al.* (2016). Protein-retention expansion microscopy of cells and tissues labeled using standard fluorescent proteins and antibodies. Nat Biotechnol 349, 987–992.
Truckenbrodt S, Sommer C, Rizzoli SO, Danzl JG (2019). A practical guide to optimization in X10 expansion microscopy. Nat Protoc 14, 832–863.
Wen G, Vanheusden M, Acke A, Valli D, Neely RK, Leen V, Hofkens J (2020). Evaluation of direct grafting strategies via trivalent anchoring for enabling lipid membrane and cytoskeleton staining in expansion microscopy. ACS Nano 14, 7860–7867.
Wu X, Hammer JA (2021). ZEISS Airyscan: Optimizing usage for fast, gentle, super-resolution imaging. Methods Mol Biol 2304, 111–130.
Zhao Y, Bucur O, Irshad H, Chen F, Weins A, Stancu AL, Oh E-Y, DiStasio M, Torous V, Glass B, *et al.* (2017). Nanoscale imaging of clinical specimens using pathology-optimized expansion microscopy. Nat Biotechnol 358, 757–764.